

Materials Horizons

Accepted Manuscript

This article can be cited before page numbers have been issued, to do this please use: Q. Zhou, M. Chen, J. Lu, B. Sheng, J. Chen, Q. Zhang and X. Han, *Mater. Horiz.*, 2025, DOI: 10.1039/D4MH01869A.



This is an Accepted Manuscript, which has been through the Royal Society of Chemistry peer review process and has been accepted for publication.

Accepted Manuscripts are published online shortly after acceptance, before technical editing, formatting and proof reading. Using this free service, authors can make their results available to the community, in citable form, before we publish the edited article. We will replace this Accepted Manuscript with the edited and formatted Advance Article as soon as it is available.

You can find more information about Accepted Manuscripts in the [Information for Authors](#).

Please note that technical editing may introduce minor changes to the text and/or graphics, which may alter content. The journal's standard [Terms & Conditions](#) and the [Ethical guidelines](#) still apply. In no event shall the Royal Society of Chemistry be held responsible for any errors or omissions in this Accepted Manuscript or any consequences arising from the use of any information it contains.

Wider impact

Solid-state batteries have been regarded as one of the most promising candidates for replacing the conventional lithium-ion batteries, due to their intrinsic safety and high energy density. One enabling technology is solid-state electrolytes (SSEs), among which, solid polymer electrolytes (SPEs) show great promise because of their flexibility, low cost and compatibility with roll-to-roll techniques. Due to the lack of fundamental insights and understanding of the solvation structure between Li salt, polymer chains, and residual solvents, however, the current SPEs are challenged by the low ambient ionic conductivity and poor interface stability that restricts its practical application in a wide temperature range. Therefore, it is urgent to present a review on the Li⁺ coordination structure, ionic transport mechanism and resultant interphases, which is crucial to enable high rate and long-term cycling for solid-state batteries. The advancement will further boost the design and research of high energy density solid-state batteries.



Data availability

View Article Online
DOI: 10.1039/D4MH01869A

No primary research results, software or code have been included and no new data were generated or analysed as part of this review.



Wide-temperature solid polymer electrolytes: Li⁺ coordination structure, ionic transport and interphases

Qingqing Zhou¹, Minfeng Chen¹, Junjie Lu¹, Bifu Sheng¹, Jizhang Chen^{1*}, Qiaobao Zhang^{2*}, and Xiang Han^{1*}

1. College of Materials Science and Engineering, Co-Innovation Center of Efficient Processing and Utilization of Forest Resources, Nanjing Forestry University, Nanjing 210037, Jiangsu, China

2. State Key Laboratory of Physical Chemistry of Solid Surfaces, College of Materials, Xiamen University, Xiamen, Fujian 361005, China

*Corresponding authors: Xiang Han (hanxiang@njfu.edu.cn); Jizhang Chen (chenjizhang@njfu.edu.cn); Qiaobao Zhang (zhangqiaobao@xmu.edu.cn)

Abstract: Solid-state batteries have gradually become a hotspot for the development of lithium-ion batteries due to their intrinsic safety and potential high energy density, among which, solid polymer electrolytes (SPEs) have attracted much attention due to the advantages of low cost, good flexibility and scalability for commercial application. However, the low ionic conductivity at room temperature, low mechanical strength and unstable interfaces of SPEs hinder further practical applications. In this paper, the modulation of Li coordination structure and different ion transport channels in wide-temperature range are reviewed. In addition, the effects of Li coordination structure on the electrolyte/electrode interfaces/interphases and electrochemical performance are also presented. Furthermore, future research directions including coordination structure, ions transport, manufacturing techniques and full cell performance are summarized and outlooked, which will provide general principles to design safe and high-performance solid-state lithium batteries.

Keywords: lithium-ion batteries; solid polymer electrolyte; Li coordination structure; ion transport; solid electrolyte interphase (SEI)



Table of Contents

View Article Online
DOI: 10.1039/D4MH01869A

1 Introduction	4
2 Mechanisms of multiphase and multiscale ion transport in solid-state batteries	9
2.1 Comparison of ionic conductivity of polymer-inorganic solid electrolytes	11
2.2 Ion coordination and transport mechanisms at molecular level	13
2.3 Traditional ion transport mechanism of polymer-inorganic SSE	14
2.4 New mechanism on ion transport of polymer-inorganic SSE	15
2.4.1 Inorganic fillers construct ion transport channel	15
2.4.2 Space charge layer (SCL) effect	16
2.4.3 Lithium salt coordinating with residual solvent generates new lithium ions transport channels	17
2.5 Challenges in lithium-ion transport and interfaces stability	19
3. Regulation strategies for improving the ionic conductivity of polymer-inorganic SSEs	21
3.1 High concentration and locally high concentration SPEs	21
3.2 Addition of inorganic nanofillers	22
3.3 Involvement of residual solvents in Li coordination	23
3.3.1 Strong interaction between DMF and high dielectric PVDF-based SPEs	24
3.3.2 Nanoscale inorganic fillers anchoring solvents	26
4 Electrode-electrolyte interfaces	28
4.1 Electrolyte-cathode interface	29
4.1.1 Liquid, sulfide, oxide and polymer electrolytes with cathode interfaces	29
4.1.2 LiF-rich interface from liquid to solid electrolytes	30
4.2 Electrolyte-anode interface	32
4.2.1 Graphite anode	33
4.2.2 Lithium metal anode	34
4.2.3 Silicon anode	37
4.3 Advanced characterization techniques on lithium-ion transportation and interphases	40
4.3.1 2D NMR	41
4.3.2 Cryo-TEM	43
4.3.3 Raman spectrum	46
4.3.4 Nano-IR	48
5 Electrochemical performances	49
5.1 High voltage performance	51
5.2 High loading capacity	53



5.3 Wide temperature range 54
 5.3.1 Adding fillers to reduce temperature sensitivity 55
 5.3.2 Structural modifications to provide functional properties 56

 5.4 Low external pressure 57
6 Summary and outlook 60
References 62

[View Article Online](#)
DOI: 10.1039/D4MH01869A

Open Access Article. Published on 11 February 2025. Downloaded on 2/21/2025 12:28:07 PM.
This article is licensed under a Creative Commons Attribution-NonCommercial 3.0 Unported Licence.

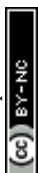


1 Introduction

View Article Online
DOI: 10.1039/D4MH01869A

In recent years, lithium-ion batteries (LIBs) have been widely applied in electric vehicles, large-scale energy storage and power grids due to their advantages of high operating voltage, high energy density, the ability to charge and discharge rapidly, long cycle life and wide operating temperature range. Conventional lithium-ion batteries normally use liquid electrolytes with good ionic conductivity (10^{-3} – 10^{-2} S cm⁻¹ at a concentration of 1 M at room temperature), good wettability with electrodes and diaphragms, and low internal resistance of the battery as well as electrode/electrolyte interface resistance[1],[2]. Generally, the liquid electrolytes comprise of carbonate-based liquid electrolytes such as ethylene carbonate (EC), dimethyl carbonate (DMC) and diethyl carbonate (DEC), and lithium salts are generally LiPF₆[3], which have better oxidation resistance but are less compatible with lithium metal anodes. Ether liquid electrolytes using ether solvents such as ethylene glycol dimethyl ether (DME) are more compatible with lithium metal anode, but the oxidative decomposition voltage is low (<4 V)[4]. Some studies have proposed new additives with higher oxidation voltage, such as fluorinated ethylene carbonate (FEC)[5], β-fluorosulfone[6]. All of these electrolytes are liquid electrolytes in organic systems, which are less safe because organic solvents are flammable (the ignition point is generally within the range of 24–45 °C, with a small portion above 45–65 °C) and batteries with liquid electrolytes suffer from leakage problems.

State-of-the-art lithium-ion batteries have approached their energy density limits and are challenged by the growing demands of today's energy storage and power applications. In particular, the future energy storage market for electric vehicles requires batteries with specific energy greater than 500 Wh kg⁻¹ (to support a range of 1000 km) and at a lower cost[7]. The need for a battery to be more cost-effective has been identified as a major challenge. Interest in all-solid-state lithium-ion batteries (ASSLIBs) using solid-state electrolytes (SSEs) is growing due to their much-improved safety and performance compared to conventional lithium-ion batteries using flammable organic liquid electrolytes. The development of LIBs has experienced a



renaissance from lithium metal batteries (LMBs) based on lithium metal anodes to lithium batteries using embedded lithium composite electrodes to LMBs. LMBs, with lithium metal as the anode material, have higher energy density and specific capacity, and theoretically can provide longer range and higher performance. However, LMBs are prone to dendrite growth, short circuits, and safety issues during charging and discharging, leading to limitations in their commercial application, and there is an urgent need to develop solid-state LMBs with higher safety.

Currently common SSEs mainly include sulfide electrolytes, oxide electrolytes, halide electrolytes and polymer electrolytes. The review classifies SSEs according to their types, give an overview of the development of SSEs, and also compares the performance of various SSEs, as shown in Fig. 1 and 2.

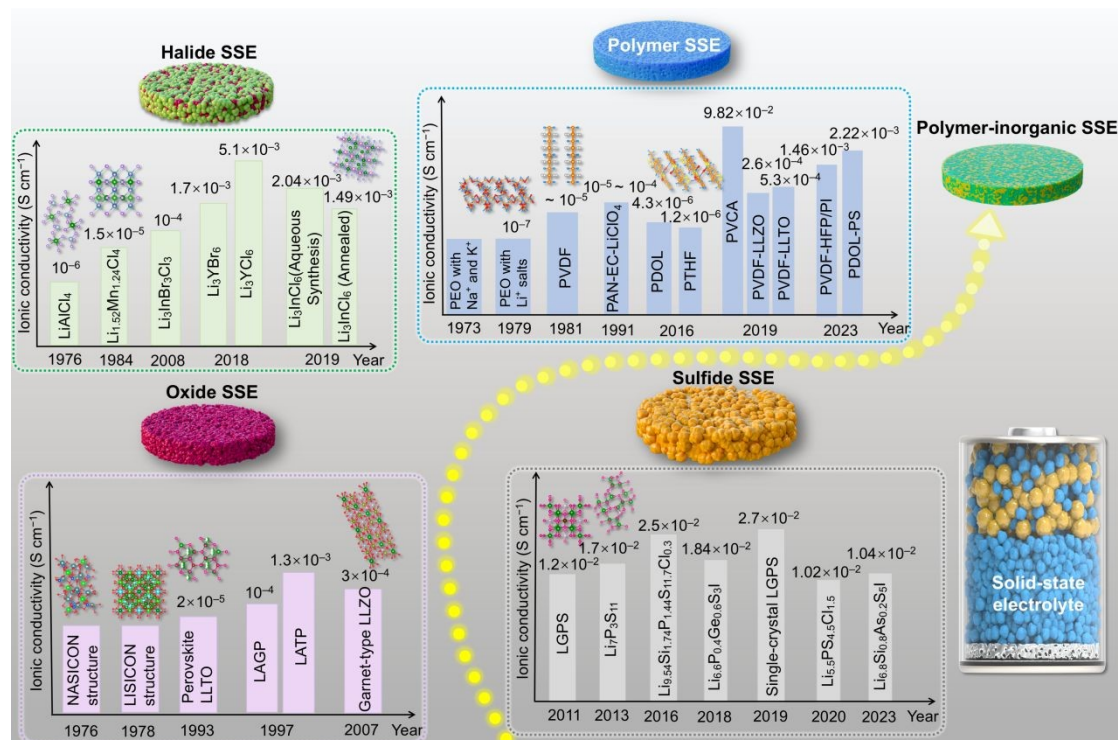


Fig. 1 A chronology of the development of typical SSEs.

In the 1970s, the discovery of new-type inorganic lithium superionic conductor (LISICON)[8] and sodium superionic conductor (NASICON)[9] opened new windows for SSEs. LISICON and NASICON as typical structures inspired many derivations and new design of oxide SSEs, such as $\text{Li}_{1+x}\text{Al}_x\text{Ge}_{2-x}(\text{PO}_4)_3$ (LAGP)[10] and $\text{Li}_{1+x}\text{Al}_x\text{Ti}_{2-x}(\text{PO}_4)_3$ (LATP)[11]. Other structures such as perovskites $\text{Li}_{0.34}\text{La}_{0.51}\text{TiO}_{2.94}$



(LLTO)[12] and garnet-based SSEs $\text{Li}_7\text{La}_3\text{Zr}_2\text{O}_{12}$ (LLZO)[13] were proved the ability for ionic conduction in 1993 and 2007, respectively. Oxide electrolytes have a wider electrochemical stability window and higher oxidative stability than sulfides. However, the room-temperature ionic conductivity of oxide electrolytes is generally lower than that of sulfides, and their larger crystal boundary resistance also limits their ionic conductivity[14],[15].

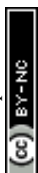
Sulfide SSEs are derived from oxide SSEs. In 2008, scholars at the University of Siegen in Germany discovered the sulfur germanium silver type electrolyte $\text{Li}_6\text{PS}_5\text{X}$ ($\text{X}=\text{Cl}, \text{Br}, \text{I}$)[16]. In 2011, scholars from Tokyo Institute of Technology synthesized $\text{Li}_{10}\text{GeP}_2\text{S}_{12}$ (LGPS)[17], and its conductivity reached $1.2 \times 10^{-2} \text{ S cm}^{-1}$. The $\text{Li}_7\text{P}_3\text{S}_{11}$ [18] electrolyte reported in 2013 has an ionic conductivity of $1.7 \times 10^{-2} \text{ S cm}^{-1}$. In 2016, Japan researchers discovered the LGPS-type SSE $\text{Li}_{9.54}\text{Si}_{1.74}\text{P}_{1.44}\text{S}_{11.7}\text{Cl}_{0.3}$ [19], and its bulk ion conductivity reached $2.5 \times 10^{-2} \text{ S cm}^{-1}$. Generally speaking, the high ionic conductivity of sulfide SSEs comes from S^{2-} , which has a larger ionic radius and polarizability than O^{2-} [20]. On the other hand, the electronegativity of S is small, and the interaction force between the neighboring skeleton ions is small, which is conducive to improving the concentration of free lithium ions[21],[22]. LGPS is the first solid electrolyte where the ionic conductivity at room temperature exceeds the electrolyte level, due to the three-dimensional skeleton structure of LGPS, which provides a fast transport channel for lithium ions. Moreover, the calculation results show that the activation energy of lithium ion diffusion between face-sharing tetrahedron is the lowest, LGPS and $\beta\text{-Li}_3\text{PS}_4$ structures have body-centered cubic lattice structure, and face-sharing tetrahedron occupy the whole cell, so materials with body-centered cubic lattice structure tend to have higher ionic conductivity[23]. Besides, sulfide SSEs are relatively soft, and most can achieve close contact only through simple cold pressing forming, thus showing high cold-pressed ion conductivity, which is unmatched by oxide electrolytes[24].

Halide SSEs have attracted attention because of their potentially high ionic conductivity, good deformability, and wide electrochemical window, but still suffer



from drawbacks such as poor interfacial compatibility[25]. In 1976, Weppner et al.[26] developed a typical LiAlCl_4 halide solid electrolyte for battery systems, displaying the ionic conductivity with $\sim 10^{-6} \text{ S cm}^{-1}$. Then, various Li_2MCl_4 and Li_2MBr_4 compounds[27] (where M is a transition metal) were developed to enhance ionic conductivity. In 2008, Koji Yamada et al.[28] synthesized $\text{Li}_3\text{InBr}_3\text{Cl}_3$ with the ionic conductivity of $10^{-4} \text{ S cm}^{-1}$. Until 2018, Asano et al.[29] made the significant discovery that the room temperature ionic conductivity of Li_3YCl_6 and Li_3YBr_6 halide solid electrolytes was $5.1 \times 10^{-4} \text{ S cm}^{-1}$ and $1.7 \times 10^{-3} \text{ S cm}^{-1}$, respectively. Subsequently, Sun's research group[30] achieved the synthesis of halide SSEs with high ionic conductivity ($2.04 \times 10^{-3} \text{ S cm}^{-1}$) in aqueous solutions for the first time, and halide electrolytes once again attracted extensive attention from researchers.

Polymer SSEs are made up of a polymer matrix and alkali metal salts dissolved in that polymer matrix. Solid polymer electrolytes (SPEs) offer several advantages over liquid electrolytes, including excellent processability, no leakage, high energy density, shape flexibility, and reduced reactivity to the active electrode surface[31]. In 1973, Fenton et al.[32] were the first to discover that adding alkali metal salts to poly(ethylene oxide) (PEO) gives it ionic conductivity. Later, Berthier et al.[33] suggested using lithium salt-containing PEO-based polymer electrolytes in solid-state lithium batteries. After that, other polymer electrolytes for Li^+ conduction were developed, including poly(vinylidene fluoride) (PVDF)[34], and poly(acrylonitrile) (PAN)[35], poly(dioxolane) (PDOL)[36], poly(tetrahydrofuran) (PTHF)[37], poly(vinyl chloride) (PVC)[38], etc. However, the above pure polymer solid electrolyte has low ionic conductivity at room temperature, which limits the development of solid-state batteries.



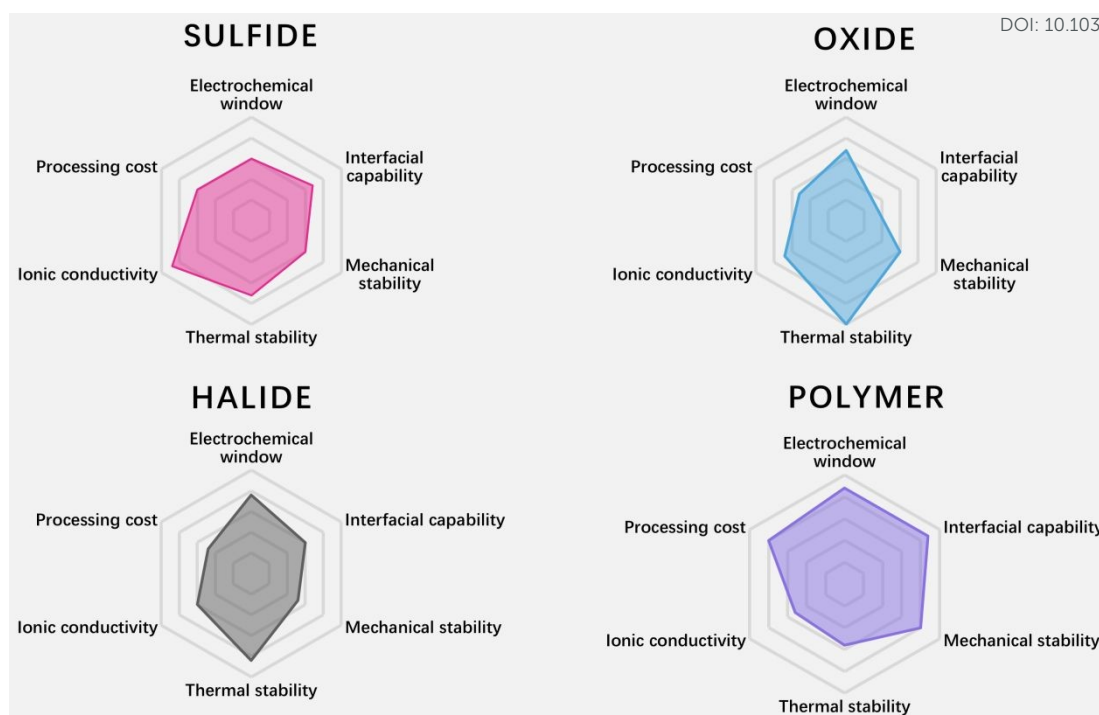
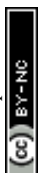


Fig. 2 Radar plots of the performance properties of Sulfide SSEs, Oxide SSEs, Halide SSEs and Polymer SSEs. (Data are from Ref.[39]–[40][41])

In recent years, for the development of solid polymer electrolytes (SPEs), researchers tend to compound them with inorganic substances. The glass transition temperature of polymer electrolyte can be effectively reduced by doping inert filler in polymer electrolyte, and the mechanical properties of electrolyte can be effectively improved by adding inorganic filler. In the past decade, researchers have turned more attention to active fillers, such as LATP, $\text{Li}_{6.75}\text{La}_3\text{Zr}_{1.75}\text{Ta}_{0.25}\text{O}_{12}$ (LLZTO) and so on. The active filler is the filler involved in the conductive process, because it can provide conductive lithium ions, lithium ions can not only be transferred in the polymer phase, but also in the active filler phase, so that the conductivity of the polymer electrolyte will be effectively improved.

This paper reviews the modulation of coordination structures, ion transport mechanisms and interfacial film-forming behavior in polymer-inorganic electrolytes in solid-state batteries under a wide temperature domain. Firstly, the ion transport mechanism in solid-state batteries is outlined, and the coordination structures and ion transport channels of polymer electrolytes are introduced, as well as the effects of lithium salt concentration, solvent type and inorganic nanofillers on lithium-ion



transport. Then, the effects of coordination structures on electrolyte interfaces and electrochemical properties are discussed, as well as some advanced characterization tools. Finally, a comprehensive summary and outlook of future research directions are given.

2 Mechanisms of multiphase and multiscale ion transport in solid-state batteries

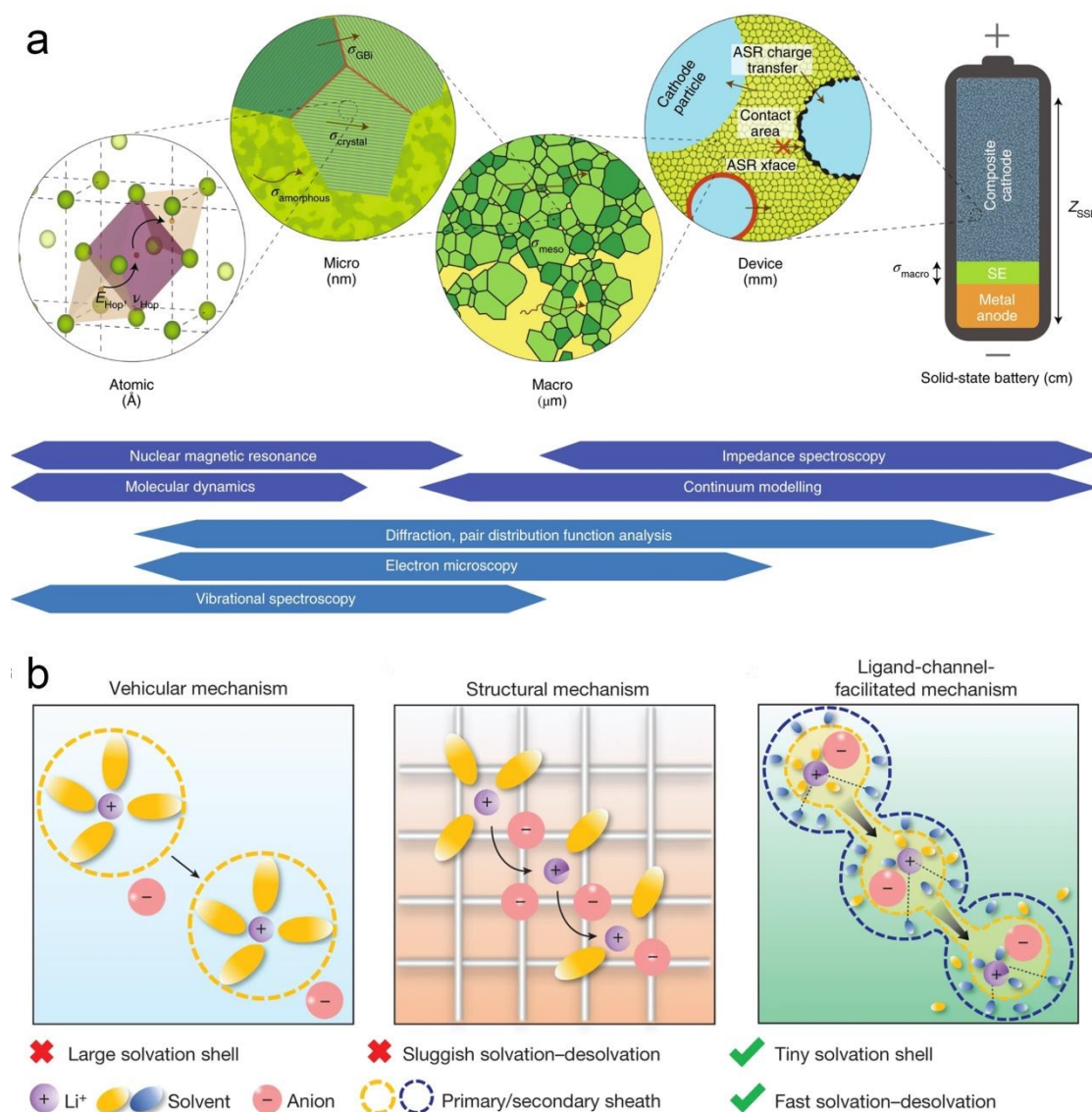


Fig. 3 Multiphase and multiscale ion transport mechanism: a) Multiscale and corresponding characterization techniques. Reproduced with permission from ref. [39]. Copyright 2019, Spring Nature. Arrows denote the transport of mobile cations in the SSE framework (in green). The major descriptors relating to ion transport are highlighted at each length scale: energy (E_{Hop}) and frequency of hops (v_{Hop}) at the atomic scale; the conductivities (σ_i) and area-specific resistances (ASR_i) of defining features at larger scales; culminating in total device impedance, Z_{SSB} . techniques utilised to directly probe ion transport (that is, quantitatively determine the above descriptors; in dark blue) and complementary methods. The techniques utilized to directly probe ion transport (that is,



quantitatively determine the above descriptors; in dark blue) and complementary methods used to aid interpretation (in light blue) are placed in their associated length scales. b) Mechanisms of ion transport in battery electrolytes. Reproduced with permission from ref. [49]. Copyright 2024, Spring Nature.

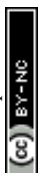
The migration of ions in solid-state batteries is a multiscale process consisting of mechanisms at different length scales, from the atomic scale to the device scale, as shown in Fig. 3a[39]. At the atomic scale, mobile cations (e.g. Li^+ , Na^+ or Mg^{2+}) diffuse in the solid along favorable migration paths and can be regarded as ionic leaps between the basal stable sites and intermediate sub-stable sites of the backbone consisting of anions (e.g. O^{2-} , S^{2-} , or polyanionic parts). These centers and their energies are mainly determined by their local ionic coordination, i.e. the bonding environment, which is often tetrahedral or octahedral in crystalline compounds. Thus, the migration path of ions through a material is a function of the availability and interconnectivity of the different positions defined by the anionic arrangement. Compositional or structural inhomogeneities exhibited on the nano- to micrometer scale tend to dominate macroscopic ionic conductivity, whether it is a beneficial[42]–[43][44] or harmful[45],[46]. Prime examples of microstructural features are grain boundaries, i.e., contact surfaces between differently orientated microcrystals in polycrystalline samples, which can be quite different from bulk crystals in terms of structure and composition. Grain boundaries have been shown to increase the resistance to ion migration in most cases, which makes them undesirable in macroscopic samples. On the macroscopic scale, the ionic conductivity of solid materials is usually measured on macroscopic samples (usually particles) by impedance spectroscopy. Impedance spectroscopy is sensitive to all of the above structural features on all length scales and allows the measurement of the total conductivity of macroscopic ions. The critical impedance value Z_{Device} is obtained at the device level, which includes the contribution of materials other than the solid electrolyte, in particular the conductivity of interfacial phases that may be formed. Most solid electrolytes are unstable and decompose on contact with the electrode material. The interfaces formed are usually resistant to ion transport and are one of the main barriers to ion conduction[47],[48].



It is generally accepted that lithium ions are transported in liquid electrolytes by two main modes, vehicular transport and structural transport (Fig. 3b)[49]. In vehicular transport, ions carry a layer of solvent molecules with them as they move, and larger solvent molecules can impede transport. In structural transport, ions form complexes with one or more solvent molecules and can therefore jump between molecules. Lu et al. found that very small solvent molecules can form two layers of sheaths around the lithium ion[49]. The tiny inner sheath contains solvent molecules and counterions of lithium ions, and the outer sheath contains only solvent molecules; these solvent molecules pull the lithium ions out of the inner sheath, thus forming channels through which lithium ions can be transported, improving the mobility of the ions.

2.1 Comparison of ionic conductivity of polymer-inorganic solid electrolyte

SPEs exhibit remarkable processability and flexibility[50],[51]. Although they may not wet the electrodes as effectively as liquid electrolytes (LEs), their flexibility allows for favorable contact with the electrodes. Certain polymers can be in situ polymerized, leading to even better electrode/electrolyte interfacial properties. However, their soft nature also makes them unsatisfactory for suppressing lithium dendrites[50]. Also, their ionic conductivity (ranging from 10^{-8} to 10^{-6} S cm^{-1} at RT) is far below the practical application requirements[52]. Even though SPEs have a wider electrochemical stability window than LEs, they still face challenges in matching the high-voltage cathodes. Furthermore, some polymers, like PAN and PVDF, are unstable with the lithium metal anodes due to their specific functional groups[53]. In order to enhance the comprehensive properties of polymer-based SSE, it is usually combined with inorganic materials to prepare polymer-inorganic SSE. Polymer-inorganic SSEs inherit the flexibility and scale-up processability of the polymer component and, hence, could be compatible with the large-scale and roll-to-roll fabrication processes used for conventional Li-ion batteries. In addition, polymer-inorganic SSEs might achieve enhanced ionic conductivity and stability, resulting from the inorganic component and synergistic interactions between the polymer and inorganic phase, as discussed below[54].



In addition, research on polymer-inorganic composite solid electrolytes has been more and more extensive in recent years. Table 1 summarizes the ion conductivity, ion transfer number and electrochemical window of some reported polymer-inorganic solid electrolytes.

Table 1 The ionic conductivity, Li⁺ transfer number (t_+) and electrochemically stable window (ESW) of several polymer-inorganic solid electrolytes.

Type	Polymer matrix	Inorganic filler	T/°C	σ (S cm ⁻¹)	t_+	ESW/V	References
Inert fillers	PEO/LiTFSI	Al ₂ O ₃	60	1.83×10^{-3}	-	4.9	[56]
	PEO/LiClO ₄	SiO ₂	60	1.2×10^{-3}	-	5.5	[57]
	PEO/LiClO ₄	TiO ₂	40	$\sim 10^{-4}$	0.47	5	[58]
	PAN/LiClO ₄	ZrO ₂	25	1.16×10^{-3}	-	-	[59]
	PAN/LiTFSI	SiO ₂	30	8.5×10^{-5}	0.47	4.8	[60]
	PAN/LiClO ₄	α -Al ₂ O ₃	RT	5.7×10^{-4}	0.33	-	[61]
Active fillers	PAN/LiClO ₄	LLZTO	25	1.18×10^{-3}	-	-	[59]
	PAN/LiClO ₄	LLTO	30	6.05×10^{-5}	0.42	-	[62]
	PEO/LiTFSI	Ga-LLZO	30	7.2×10^{-5}	0.39	4.6	[63]
	PEO/LiTFSI	LLZTO	30	3.16×10^{-6}	-	4.6	[64]
	PEO/LiTFSI	LAGP	30	5×10^{-5}	-	5.12	[65]
	PEO-PVDF/LiTFSI	LLZO	30	4.2×10^{-5}	-	-	[66]
	PVDF/LiFSI	BaTiO ₃ -LLTO	25	8.2×10^{-4}	0.57	-	[67]
	PVDF/LiFSI	MoSe ₂	25	6.4×10^{-4}	-	4.7	[68]
PVDF-HFP/LiTFSI	LLZTO	60	8.2×10^{-4}	0.26	4.7	[55]	
In-situ polymerization	PDOL/LiTFSI	YSZ	20	2.75×10^{-4}	0.65	4.9	[69]
	PDOL/LiTFSI	PS	30	2.2×10^{-3}	0.88	5.2	[70]



P(DOL-TXE) /LiTFSI-LiDFOB	SN	RT	4.06×10^{-4}	0.881	5.1	View Article Online DOI: 10.1039/D4MH01869A [71]
PTHF/LiClO ₄	BF ₃	60	2.3×10^{-4}	-	4.5	[72]

2.2 Ion coordination and transport mechanisms at molecular level

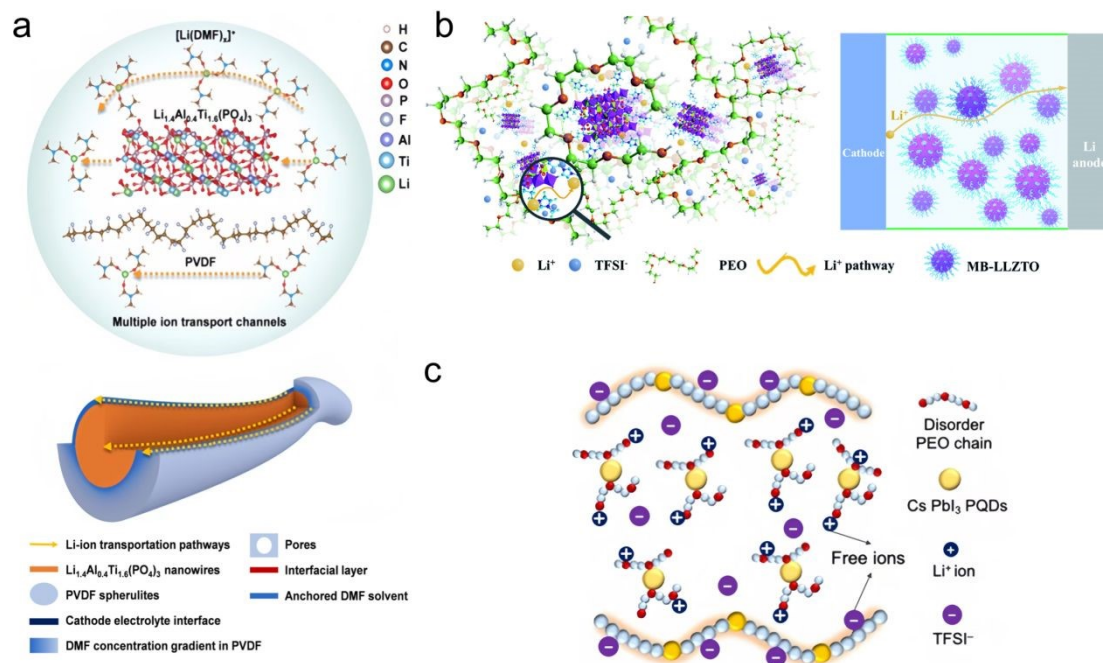
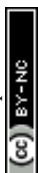


Fig. 4 a) Li-ion transport mechanism and multiple Li-ion transport channels in PVLN-15 electrolyte. Reproduced with permission from ref. [73]. Copyright 2021, Wiley. b) Diagram of the Li^+ diffusion pathway in the MB-LLZTO CPE. Reproduced with permission from ref. [74]. Copyright 2019, Royal Society of Chemistry. c) Schematic illustration of LEHE electrolyte with disorder PEO chain and even more free ions through CsPbI_3 quantum strengthening PEO-LITFSI complexes. Reproduced with permission from ref. [75]. Copyright 2024, Elsevier.

In SPEs, the interaction between ions and polymer chains is very important. Ions can form coordination complexes with polar groups in the polymer chain, and this coordination not only changes the conformation of the polymer, but also provides a channel for the movement of ions, whose coordination state determines their behavior and migration ability in the polymer matrix. He et al.[73] found that the DMF-coated nanowires together with PVDF polymer matrix create multiple and synergistic ceramic-polymer-liquid Li-ion transport channels to greatly enhance the ion transport efficiency (Fig. 4a). Wen et al.[74] designed a molecular brush nanoparticle anchored to the surface of LLZTO (MB-LLZTO) to prepare a composite solid electrolyte, as shown in Fig. 4b, the binding of MB-LLZTO to PEO alters the diffusion path of lithium ions,



and the fast ionic conductivity of the LLZTO surface improves the ionic conductivity by an order of magnitude. Yang et al.[75] designed a low enthalpy and high entropy electrolyte, as shown in Fig. 4c, and found that CsPbI₃ perovskite quantum dots largely destroyed the polymer chain, inhibited the crystallization of the polymer, adjusted the molecular orientation of the polymer, and enhanced its degree of disorder. This electrolyte inherently produces significant free ions and high mobility, allowing it to effectively drive lithium-ion storage.

2.3 Traditional ion transport mechanism of polymer-inorganic SSE

The transport mechanisms of lithium ions in polymer-based electrolytes have been the subject of extensive research, and Fig. 5a outlines several key findings that have elucidated traditional ion transport in SPEs at the microscopic level over the past 40 years[76]. As early as 1970, Armand et al. predicted that the movement of chain segments of the polymer backbone was related to the transport of ionic substances, especially for Li⁺, as shown in Fig. 5b[77]. In 1980, Berthier et al.[33] demonstrated using solid state NMR techniques that ionic transport in PEO-based SPE systems (usually "salts in polymers") occurs mainly in the amorphous regions.

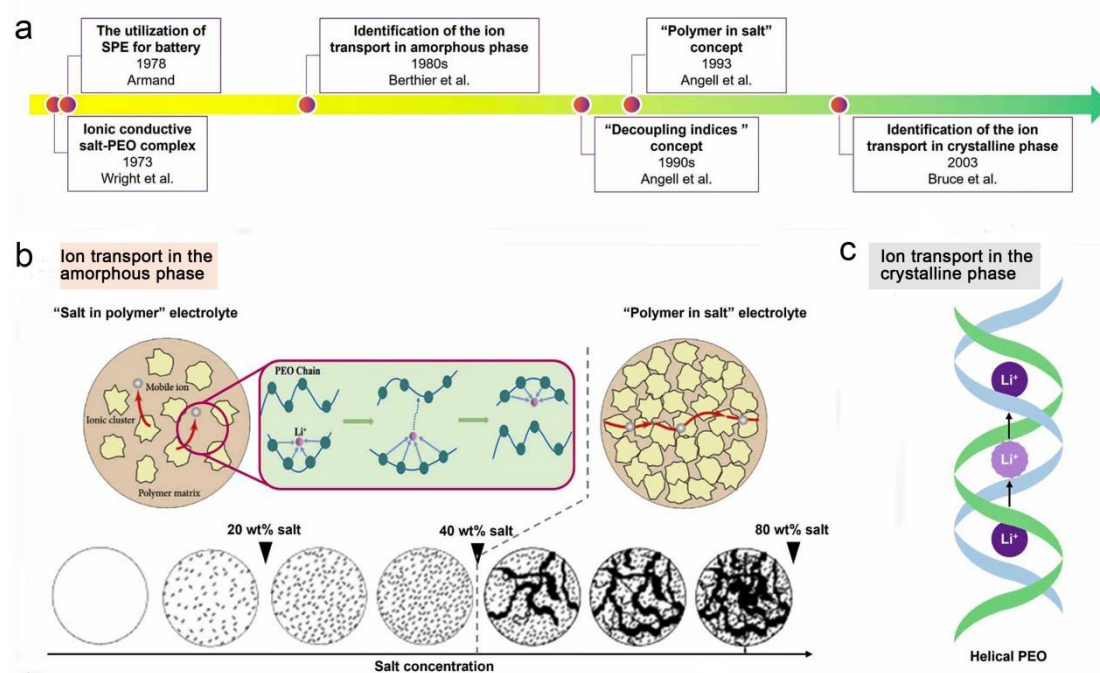


Fig. 5 Transport behaviors of ionic species in SPEs. Reproduced with permission from ref. [76]. Copyright 2022, IOP Publishing. a) Evolution progress of lithium-ion transport mechanism in SPEs electrolyte. b) Mechanism of ion transport in the amorphous phase of SPEs. c) Mechanism of ion transport in the crystalline phase of SPEs.



transport in the crystalline phase of SPEs.

From another perspective, Stoeva et al. proposed that the crystalline phase of PEO-based SPEs has ionic conductivity with a well-defined microstructure (Fig. 5c)[78]. For the crystalline phase LiAsF₆/PEO electrolyte, the relatively fast diffusion of Li⁺ is achieved by ionic substance hopping without involving the movement of the PEO chain segments (the diffusion paths are indicated by pink circles in Fig. 5c), and the PEO substrate remains "fixed" during the ionic conduction process. In contrast, the ionic conductivity of the crystalline LiAsF₆/PEO electrolyte is almost an order of magnitude higher than that of the amorphous LiAsF₆/PEO electrolyte. However, these crystalline-phase SPEs may achieve high ionic conductivity through low molecular weight PEO (<5000 g mol⁻¹), but such polymers provide little self-supporting membranes, which hampers their practical application in lithium batteries[78]–[79][80].

Since the 1990s, Angell et al.[81] systematically investigated the ion transport behavior of PEO-based electrolyte systems and revealed that Li⁺ transport is highly coupled to the motion of the polymer chain segments. 1993, Angell et al. proposed the concept of "polymer-in-salt" electrolytes, in which large amounts (>50 wt.%) of lithium salts with low melting points and high dissociation properties are used to form "decoupled" systems of SPEs[82]. In this case, the transport of Li⁺ does not depend on the segmental motion of the polymer chains.

Smooth PEO is a semi-crystalline helical polymer with a degree of crystallinity (>60%) due to its regular and highly ordered structure[83],[84]. As mentioned above, ion transport in SPEs is largely dependent on chain segment movement and local relaxation of the polymer, with Li⁺ transport occurring mainly in the amorphous regions of the SPEs[85]–[86][87][88]. As a result, the ionic conductivity of PEO-based SPEs is typically lower than 10⁻⁵ S cm⁻¹ at RT[88], which limits its large-scale application in solid-state LMBs.

2.4 New mechanism on ion transport of polymer-inorganic SSE

2.4.1 Inorganic fillers construct ion transport channel

Solvation structure of Li⁺ is important to ion transport in polymer-inorganic SSE.



There are two steps during the transportation of Li^+ inside the electrolyte: (i) solvation of Li^+ by the solvent molecules and (ii) migration of the solvated ions. These two steps determine ionic conductivity[89]. The ion transport slows down as an increase in the rigidity of the solvation shell of Li^+ ions, which is due to an increase in the drag against the motion of lithium-solvents complexes[90]. Zheng and his colleague's studies Li-ion pathways within LLZO-PEO (LiTFSI) composite electrolytes of different LLZO contents, as shown in the Fig. 6a[91]. To summarize, with low LLZO content (<20 wt.%), LLZO-PEO (LiTFSI) composites behave as a polymer electrolyte modified by LLZO. On increasing LLZO amount to a critical point, LLZO particles connect to form a percolated network; thus, LLZO-PEO (LiTFSI) composites function as a ceramic electrolyte. However, the ceramic particles are diluted by polymers, and as a result, ceramic electrolytes composed of loose particles exhibit much lower ionic conductivity compared with dense ceramic pellets. Moreover, bulk LLZO particles block Li-ion transport through the polymer matrix. Li transport pathways transition from the PEO matrix to the percolated LLZO network when the LLZO fraction in the composite electrolyte is increased to a critical point. The exact transition point varies depending on many factors, including the particle size and morphology of LLZO as well as the mixing degree of participating components. With TEGDME additive, Li-ion conduction occurs mainly through TEGDME-modified polymer phase. The presence of TEGDME additive in PEO has been shown to significantly enhance Li-ion conduction[92].

2.4.2 Space charge layer (SCL) effect

Numerous studies have shown that the SCL formed between the composite solid electrolyte phases can greatly influence the transport of lithium ions[93]–[94][95][96][97]. From a thermodynamic point of view, due to the difference in electrochemical potential between polymer and inorganic ceramic nanoparticles, lithium ions can rely on the potential of nanoparticles to migrate through the interface, and the migration of lithium ions leads to changes in ionic conductivity at the interface, and in some cases even changes the crystal structure[98],[99]. When the polymer and

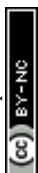
View Article Online
DOI: 10.1039/D4MH01869A



the nanoparticles come into direct contact, it causes the redistribution of lithium ions at the interface, resulting in the formation of SCL[100]. Kang et al.[67] designed a BaTiO₃ (BTO)-LLTO composite PVDF-based polymer electrolyte. Among them, BTO has a high dielectric constant and can be polarized under an applied electric field by displacement of Ti⁴⁺ and displacement of O²⁻ electrons in its octahedral structure[101],[102]. The built-in electric field generated in the dielectric material BTO may weaken the SPL limitation in the CSEs[103]–[104][105] and reduce the Li⁺ concentration[106], which may dissociate the lithium salt to produce more mobile Li⁺. Guo's group synthesized PEO: Li_{6.25}Ga_{0.25}La₃Zr₂O₁₂ (Ga-LLZO) composite polymer electrolyte by dispersing Ga-LLZO nanoparticles in PEO matrix[63]. Fig. 6c shows the evolution of the space charge region in a single Ga-LLZO nanoparticle. When the regions of space charge generated in a single nanoparticle are connected to each other, a continuous path of space charge regions can be formed. The space charge region has two effects: the ionic conductivity is affected by changing the concentration of defects in the region[107]; It provides a new kinetic pathway for ionic conductivity. It is worth nothing that highly conductive regions around isolated particles have little effect on ionic conductivity, however, if a continuous path is formed (the case above the percolation threshold), the contribution of the space charge region to ionic conductivity is significant[63]. Therefore, when the content of Ga-LLZO in PEO: Ga-LLZO composite exceeds the seepage threshold, the formed continuous path of space charge region can be regarded as a fast channel of lithium-ion transport.

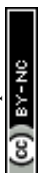
2.4.3 Lithium salt coordinating with residual solvent generates new lithium ions transport channels

Unlike the ion transport in conventional SPEs, residual solvents play a crucial role in the ion transport of vinylidene fluoride (VDF)-based SPEs. However, they also induce several problems that have long been neglected. Commonly used solvents such as N,N-dimethylformamide (DMF), N-methyl-2-pyrrolidone (NMP), and dimethyl sulfoxide (DMSO) are inherently thermodynamic unstable with lithium metal. Their side reactions with lithium metal result in the progressive formation of a thickened



interfacial corrosion layer on the lithium metal surface, leading to increased interfacial impedance. On the other hand, the constant consumption of residual solvents in VDF-based SPEs leads to a decrease in ionic conductivity and exacerbates battery polarization. Zhi et al propose a strategy to inhibit the side reactions induced by the residual solvent with electrodes in poly(vinylidene fluoride-co-hexafluoropropylene) (PVHF)-based SPE by developing fluorinated 2,2,2-trifluoro-N,N-dimethylacetamide (FDMA) as the solvent[108]. The inherent stability of fluorinated FDMA solvent with Li metal ensures the interface stability between PVHF-FDMA-SPE and Li metal. The formed $[\text{Li}(\text{FDMA})_x]^+$ solvation molecules contributed to the high ionic conductivity with a low activation energy of the PVHF-FDMA-SPE. To further understand the influence of the FDMA solvent on the ion transport mechanism of the PVHF-FDMA-SPE, molecular dynamics (MD) simulations were carried out to investigate the coordination structures (Fig. 6b). The strong peaks of the Li-O pairs at 1.93 Å indicated that both the FDMA and TFSI⁻ were coordinated with Li⁺. Notably, there is no coordination between the F atom of PVHF and Li⁺. Therefore, Li-ion transport in PVHF-FDMA-SPE mainly relies on combining residual FDMA solvent and Li salts to form a Li-FDMA-3TFSI-solvation structure. Its intermolecular interactions with the PVHF chain could transport this structure, facilitating ion conduction. The Li-FDMA-3TFSI-solvation structure transport mechanism in PVHF-FDMA-SPE is illustrated in Fig. 6b right.

View Article Online
DOI: 10.1039/D4MH01869A



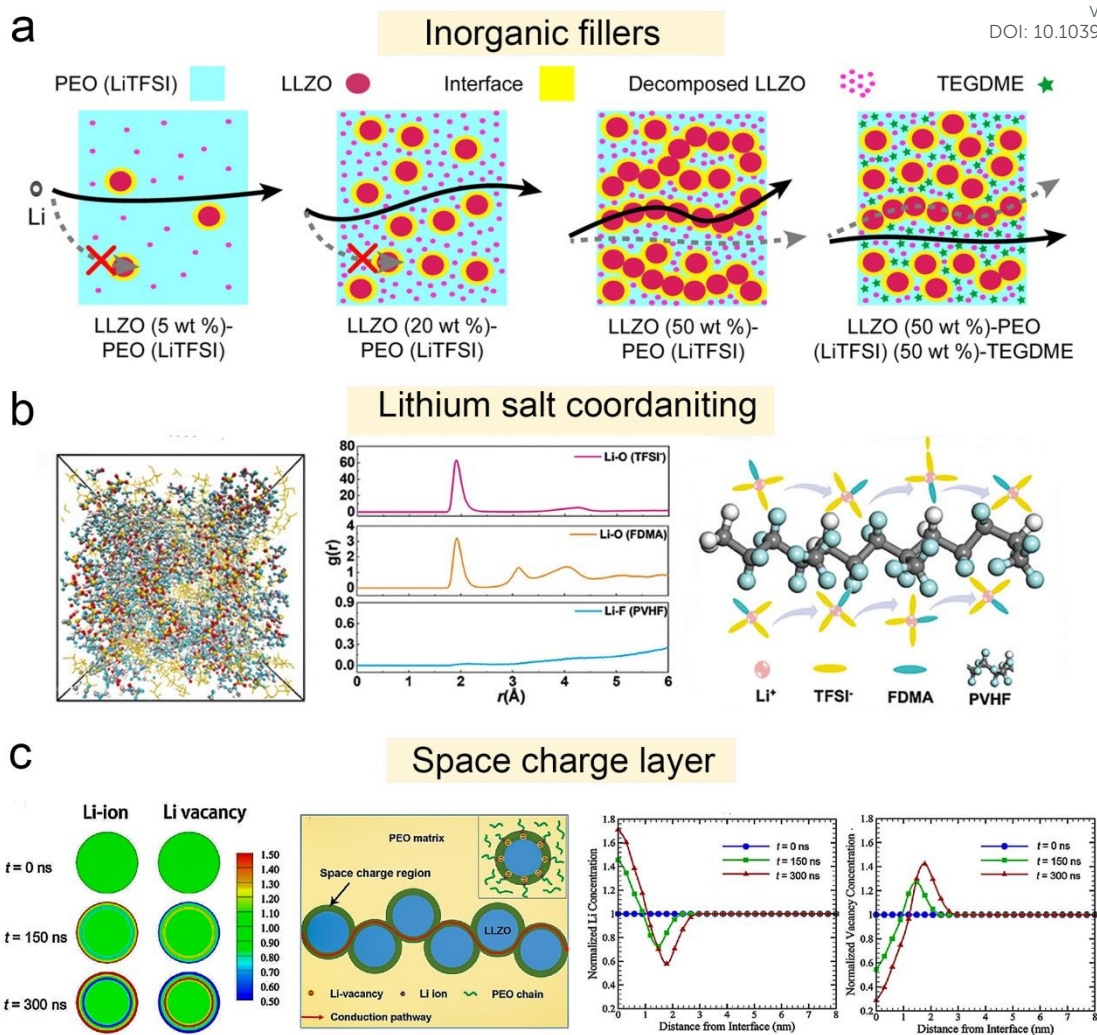


Fig. 6 Solvation structure and new ion transport mechanism of polymer-inorganic SSE. a) Schematic of Li-ion pathways within LLZO (5 wt %)-PEO (LiTFSI), LLZO (20 wt %)-PEO (LiTFSI), LLZO (50 wt %)-PEO (LiTFSI), and LLZO (50 wt %)-PEO (LiTFSI) (50 wt %)-TEGDME composite electrolytes. Reproduced with permission from ref. [91]. Copyright 2022, IOP Publishing. b) Snapshots of the MD simulation boxes of PVHF-FDMA-SPE; radial distribution function (RDF) plots of Li-O (TFSI), Li-O (FDMA), and Li-F (PVHF); schematic diagram of Li-FDMA-3TFSI-solvation structure transportation mechanism in PVHF-FDMA-SPE. Reproduced with permission from ref. [108]. Copyright 2024, Wiley-VCH GmbH. c) Formation of the space charge region at the Ga-LLZO/PEO interface. Reproduced with permission from ref. [63]. Copyright 2019, American Chemical Society. Evolution of the normalized Li⁺ (c_{Li^+}) and vacancy concentration (c_V) from 0 to 300 ns; distributions of the lithium ion concentrations, and distributions of the vacancy concentrations from the surface to the center of the Ga-LLZO nanoparticle along the radial direction at $t = 0, 150,$ and 300 ns; schematic illustration of the fast ionic conduction pathway along the space charge regions.

2.5 Challenges in lithium-ion transport and interfaces stability

The electrolyte, which physically interacts with all other components, stands out the most distinctive component in a lithium-ion battery. In LIBs, the SPE plays an



important role of an electronically insulating separator because of its high flexibility, ease of processing, good interfacial contact, good thermal stability and high mechanical strength.

View Article Online
DOI: 10.1039/D4MH01869A

However, in the process of practical application, SPEs still face some key challenges:

(1) Low ionic conductivity at room temperature. The conduction of lithium ions in the SPE is highly coupled with the chain segment motion of the polymer, which typically has high crystallinity at RT. Thus, the ionic conductivity of the SPE is low, which seriously limits its practical application.

(2) Lithium ions transport determined by multi-factors. Different concentrations of lithium salt will affect the conductivity of electrolyte and the cycle performance of the battery. Inorganic fillers can improve the mechanical properties and conductivity of the battery, and play a certain auxiliary role in the transport of lithium ions. Additives can improve the stability of the electrolyte and the chemical activity of the electrode material, which affects the transport efficiency of lithium ions and the performance of the battery. All these factors have significant effects on lithium-ion transport.

(3) Unstable electrode/electrolyte interphases. The electrochemical window is narrow, making side reactions likely to occur at the electrode interface under high voltage.

Based on the problems mentioned above, many researchers have proposed some improvement strategies. In this review, advances addressing the issues and design strategies of polymers-inorganic SSE are summarized.



3. Regulation strategies for improving the ionic conductivity of polymer-inorganic SSEs

3.1 High concentration and locally high concentration SPEs

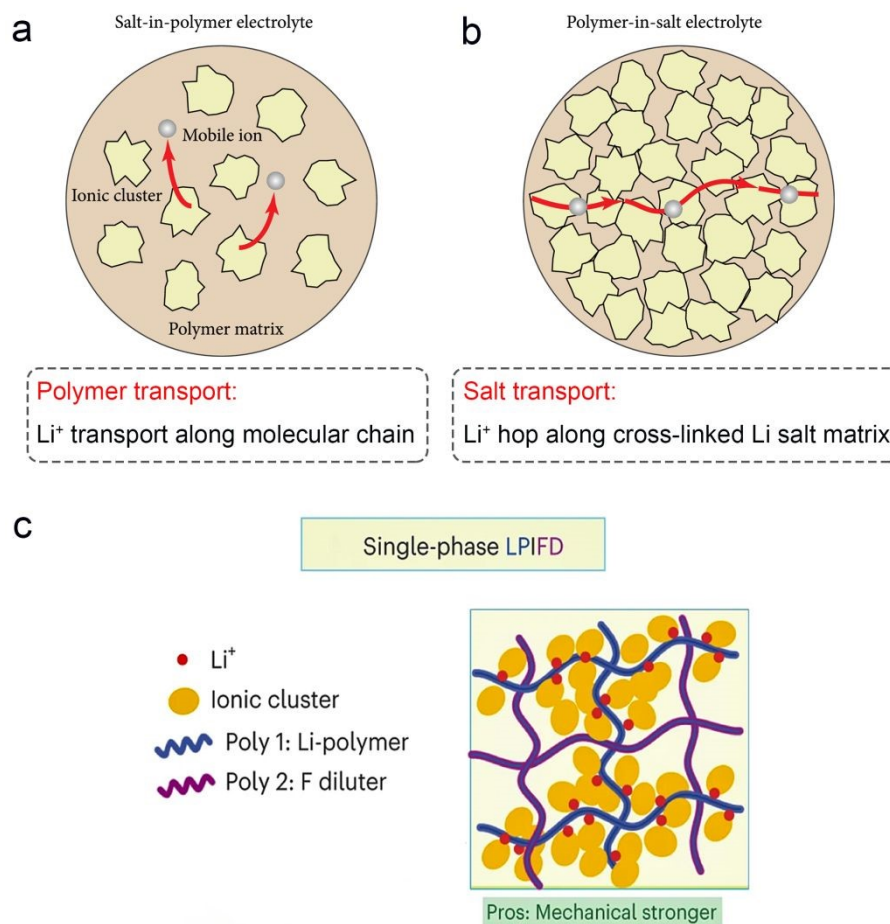
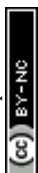


Fig. 7 Schematic illustration of lithium-ion transports. a) In a salt-in-polymer electrolyte. b) a polymer-in-salt electrolyte. Reproduced with permission from ref. [60]. Copyright 2021, Science Partner Journal. c) The single-phase LPIFD SPEs. Reproduced with permission from ref. [109]. Copyright 2024, Spring Nature.

In recent years, polymer-in-salt (PIS) solid state electrolytes with lithium salt content exceeding 50 wt.% have received renewed attention (Fig. 7a). High concentrations of lithium salts can maximally inhibit the crystallization of the polymer matrix at low temperatures, resulting in continuous amorphous regions that facilitate fast Li⁺ transport. In addition, fast ion diffusion pathways can be formed by cation/anion cluster aggregation. As a result, PIS solid electrolytes exhibit high ionic conductivity at ambient temperatures (up to 0.36 mS cm⁻¹ at 25°C) [110]. Wang's group designed a class of locally high-concentration solid polymer electrolytes based on polymer blends,

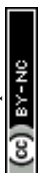


which are termed Li-polymer in F diluter (LPIFD) (Fig. 7c)[109]. The single-phase LPIFD delivers an ionic conductivity of $3.0 \times 10^{-4} \text{ S cm}^{-1}$, and enables the Li anode to reach a high coulombic efficiency of 99.1% and a critical current density of 3.7 mA cm^{-2} .

3.2 Addition of inorganic nanofillers

The structure and ion transport mechanism of organic-inorganic composite electrolytes depend on the nature and content of the inorganic materials in them. When the inorganic filler content is low, the structure and Li^+ transport mechanism of the composite electrolyte is the same as that of the all-solid polymer electrolyte[111]. The structure and Li^+ transport mechanism of composite electrolytes is the same as that of all-solid polymer electrolytes. Traditional inorganic fillers are mainly inert fillers, including SiO_2 , Al_2O_3 , TiO_2 , MgO , ZrO_2 , etc., which do not have ion transport capacity themselves, but promote the formation of penetration channels between the polymer chain and the filler by reducing the crystallinity of the polymer matrix, thus effectively improving the electrochemical performance of the composite polymer electrolyte (CPEs). Cui et al.[57] presented a method for in situ production of inorganic fillers in SPEs (Fig. 8a). Due to this in situ polymerization, SiO_2 forms a continuous dispersed phase in the polymer. As a result, more contact area is provided for Lewis's acid-based interactions. In addition, monodisperse SiO_2 effectively inhibits PEO crystallization and promotes the movement of the polymer chain segments, and as a result, SiO_2 -PEO CPE exhibits an excellent ionic conductivity of $4.4 \times 10^{-5} \text{ S cm}^{-1}$ at 30°C (Fig. 8c). Hu et al. compared the effects of different sizes of ZrO_2 (diameters of 220, 365, and 470 nm, respectively) on the formation of ion-permeable networks in PAN- LiClO_4 , and the results showed that the ionic conductivity of ZrO_2 -PAN CPEs increased with the decrease of ZrO_2 size[59]. In contrast, ZrO_2 (220 nm) can form a more effective ion transport interface. Therefore, ZrO_2 (220 nm)-PAN CPE has the best ionic conductivity of $1.16 \times 10^{-3} \text{ S cm}^{-1}$. Wu et al. constructed a crosslinked dual network structure of Al_2O_3 fillers and polymers by in situ sol-gel method (Aluminum sec-butoxide as the aluminum source) (Fig. 8b)[56]. Al_2O_3 nanoparticles were uniformly dispersed without

View Article Online
DOI: 10.1039/D4MH01869A



agglomerates and interconnected with the PEO chains to form a dual network skeleton in 3D space. The prepared CPEs not only exhibited excellent ionic conductivity but also higher Young's modulus (116.49 MPa) at RT compared to pure PEO electrolytes (60.78 MPa for pure PEO electrolytes).

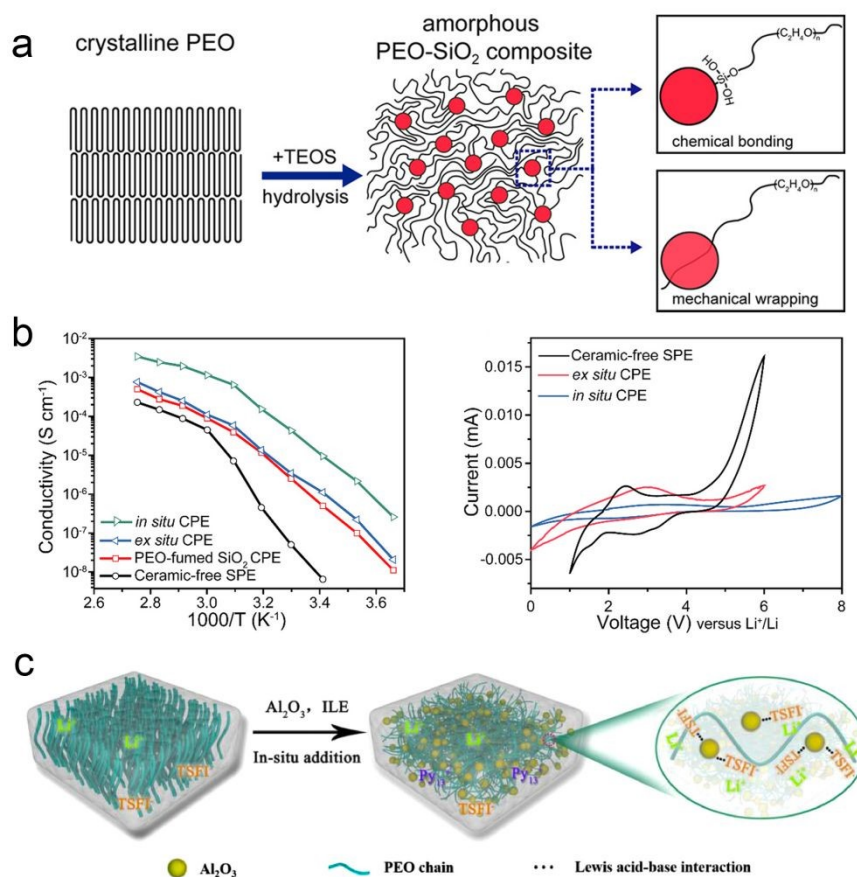


Fig. 8 The addition of traditional inorganic fillers to reduce the crystallinity. a) Schematic Figures showing the procedure of in situ hydrolysis and interaction mechanisms among PEO chains and SiO₂. b) Arrhenius plots of ionic conductivity and electrochemical stability windows of ceramic-free SPE, PEO-fumed SiO₂ CPE, ex situ CPE, and in situ CPE. Reproduced with permission from ref. [57]. Copyright 2016, American Chemical Society. c) The mechanism diagram of reducing polymer crystallinity. Reproduced with permission from ref. [56]. Copyright 2021, Elsevier.

3.3 Involvement of residual solvents in Li coordination

Recent reports have begun to focus on the use of residual solvents to improve their contact with the electrodes. It is well known that fundamental issues such as the bonding state and content of residual solvents are still controversial, but it is particularly important in terms of lithium-ion transport, interfacial stability and battery performance. Many literatures have reported excellent electrochemical performance of polymer-



based solid-state batteries, but the real working principle remains highly controversial. The focus is on whether the organic solvents (NMP, DMF, etc.) remain in the polymer's native structure. Typically, solvated complexes [solvent-Li⁺] can interact with the polymer chains to achieve high ionic conductivity and enhanced oxidation resistance of the electrolyte. However, the application reliability of such electrolytes faces the challenge of precisely controlling the effects of residual solvents to achieve stable operation. Increasingly, research focuses on limiting residual solvents to improve the electrochemical stability of polymer electrolytes. This includes adapting the preparation process, introducing inorganic fillers, and designing compatible quasi-ionic liquid/polymer electrolytes.

3.3.1 Strong interaction between DMF and high dielectric PVDF-based SPEs

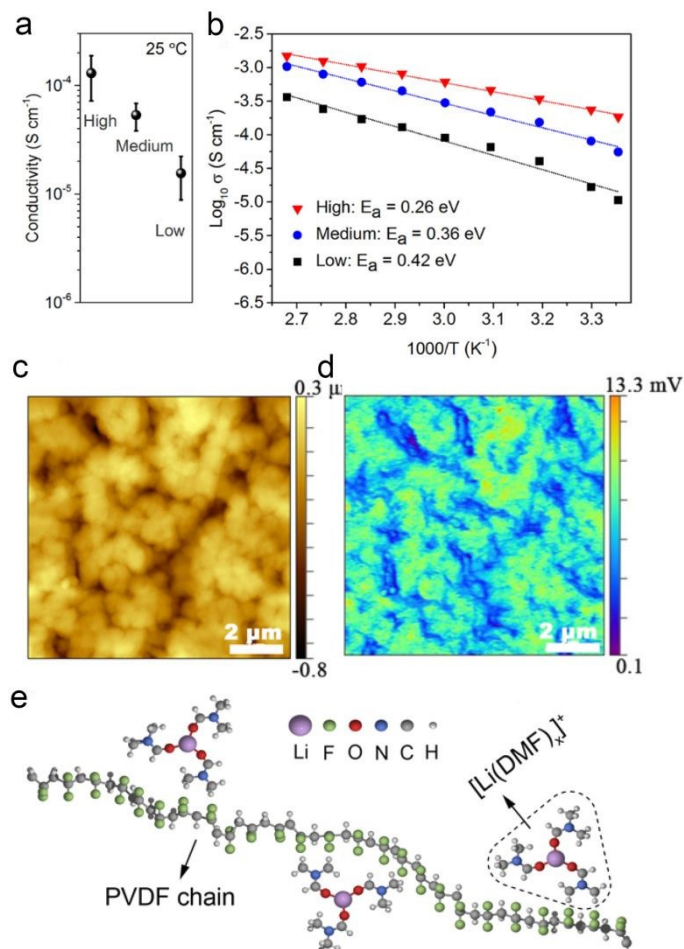


Fig. 9 Effects of residual DMF on ionic conduction in PVDF-LiFSI electrolytes: a) ionic conductivity (25 °C) and b) Arrhenius plots of the high-, medium- and low-DMF electrolytes. c) The height map of a PVDF-LiFSI electrolyte film. d) The corresponding IR intensity map of C=O vibration of DMF at 1670 cm⁻¹. e) A simple schematic diagram of the



structure of $[\text{Li}(\text{DMF})_x]^+$ ($x \leq 3.29$) in the PVDF-LiFSI electrolyte. Reproduced with permission from ref. [115]. Copyright 2020, Wiley-VCH GmbH. View Article Online
DOI: 10.1039/D4MH01869A

It was found that small amounts of DMF remained in PVDF-based electrolytes prepared with DMF as solvent. DMF helps to improve the ionic conductivity of PVDF-based electrolytes, as reported by Yao et al[112]. DMF is also essential for the interfacial stability between the electrolyte and electrode because it can be used as an electrophilic or nucleophilic agent involved in the reaction [113]. For example, PVDF-DMF solutions can react with Li metal to form a stable LiF layer, thus reducing the interfacial reaction between the electrolyte and the Li negative electrode [114]. At high current densities, DMF may be associated with the thickening of the interfacial layer between the PVDF-based electrolyte and the Li metal. The specific effect of DMF on ion transport in the PVDF-based electrolyte as well as the evolution of the electrolyte-electrode interface is still unclear. Nan's team investigated the role of residual DMF in PVDF-based electrolytes through a combination of systematic experiments and first-principles calculations[115]. They elucidated the interactions between lithium salts, DMF and PVDF chains in the electrolyte and possible ion transport mechanisms in PVDF-based solid electrolytes. Based on the residual amount of DMF, the PVDF-LiFSI electrolyte membranes can be classified into three types: high DMF content (14–17 wt.%), medium DMF content (10–14 wt.%), and low DMF content (5–10 wt.%), which are hereinafter referred to as "high DMF electrolytes", "medium DMF electrolytes" and "low DMF electrolytes", respectively. Fig. 9a shows a comparison of ionic conductivity of high, medium and low DMF electrolytes at RT. The average ionic conductivity of the high DMF electrolyte was $1.30 \times 10^{-4} \text{ S cm}^{-1}$, the highest at 25 °C, and it decreased with the decrease of DMF content. The Arrhenius plot in Fig. 9b further showed that the activation potential barriers for the migration of Li^+ were the lowest in the high DMF electrolyte and the highest in the low DMF electrolyte. The presence of DMF residue affects the structure of the PVDF-based electrolyte, thus affects the conductivity of Li^+ in the electrolyte. Fig. 9e depicts the schematic structure of DMF residues in the PVDF-LiFSI electrolyte. The nano-IR spectrogram in Fig. 10c, d shows that the bound DMF is uniformly distributed in the electrolyte. Thus, in the electrolyte, all the residual



DMF molecules bind to Li ions to form $[\text{Li}(\text{DMF})]_x^+$, and then the bound DMF molecules again interact weakly with the PVDF chains. In the absence of free solvent support, Li^+ can be transferred between the interaction sites between $[\text{Li}(\text{DMF})]_x^+$ and the PVDF chains with the help of the PVDF chains, which is analogous to the migration of lithium ions between the O-Li interaction centers in PEO-based solid electrolytes. Therefore, for electrolytes with high, medium and low DMF, the higher the DMF residue, the higher the $[\text{Li}(\text{DMF})]_x^+$ concentration, the lower the activation potential barrier for ion migration and the higher the ionic conductivity.

3.3.2 Nanoscale inorganic fillers anchoring solvents

Generally, the active fillers (chalcocite, garnet, LISICON, etc.) can form continuous ion channels in the bulk phase, which promotes the rapid ion transport and has good ionic conductivity. Liu et al. found that C-coated $\text{Li}_{1.4}\text{Al}_{0.4}\text{Ti}_{1.6}(\text{PO}_4)_3$ nanowires (C@LATP NW), as an anode filler, not only can conduct Li^+ , but also have strong adsorption effect on $[\text{Li}(\text{DMF})]_x^+$ complexes to promote the uniform diffusion of $[\text{Li}(\text{DMF})]_x^+$ in a thick anode, constructing a highly efficient Li^+ transport network and realizing the full reaction of a thick anode (Fig. 10a)[116]. Shi et al. developed a highly conductive and dielectric PVBL by compositing PVDF with coupled BaTiO_3 (BTO) and LLTO nanowires[67]. The BTO-LLTO triggered the dissociation of Li salts, facilitated the Li^+ transport and weakened the space charge layer, which resulted in the PVBL having a considerably high ionic conductivity at 25 °C ($8.2 \times 10^{-4} \text{ S cm}^{-1}$; Fig. 10b). BTO-LLTO also lowered the interfacial potential with $\text{LiNi}_{0.8}\text{Co}_{0.1}\text{Mn}_{0.1}\text{O}_2$ (NCM 811) and promoted uniform Li^+ transport for uniform Li stripping and deposition. Wu et al. obtained dense composite electrolytes by doping MoSe_2 flakes[68]. The high dielectric constant electrolyte can optimize the solvation structure to achieve high ionic conductivity and low activation energy (Fig. 10c). Zhai et al. reported a two-dimensional fluorinated graphene reinforced PVDF-HFP-LiTFSI (FPH-Li) polymer electrolyte[117]. The homogeneously dispersed fluorinated graphene has a unique grain refinement effect, which can effectively improve the mechanical properties without excessively increasing the thickness of the polymer electrolyte. The significant

View Article Online
DOI: 10.1039/D4MH01869A



reduction in polymer grain size enhances interfacial Li^+ transport and homogenizes the Li^+ flux, thereby increasing Li^+ conductivity and facilitating uniform Li -deposition/exfoliation (Fig. 10d).

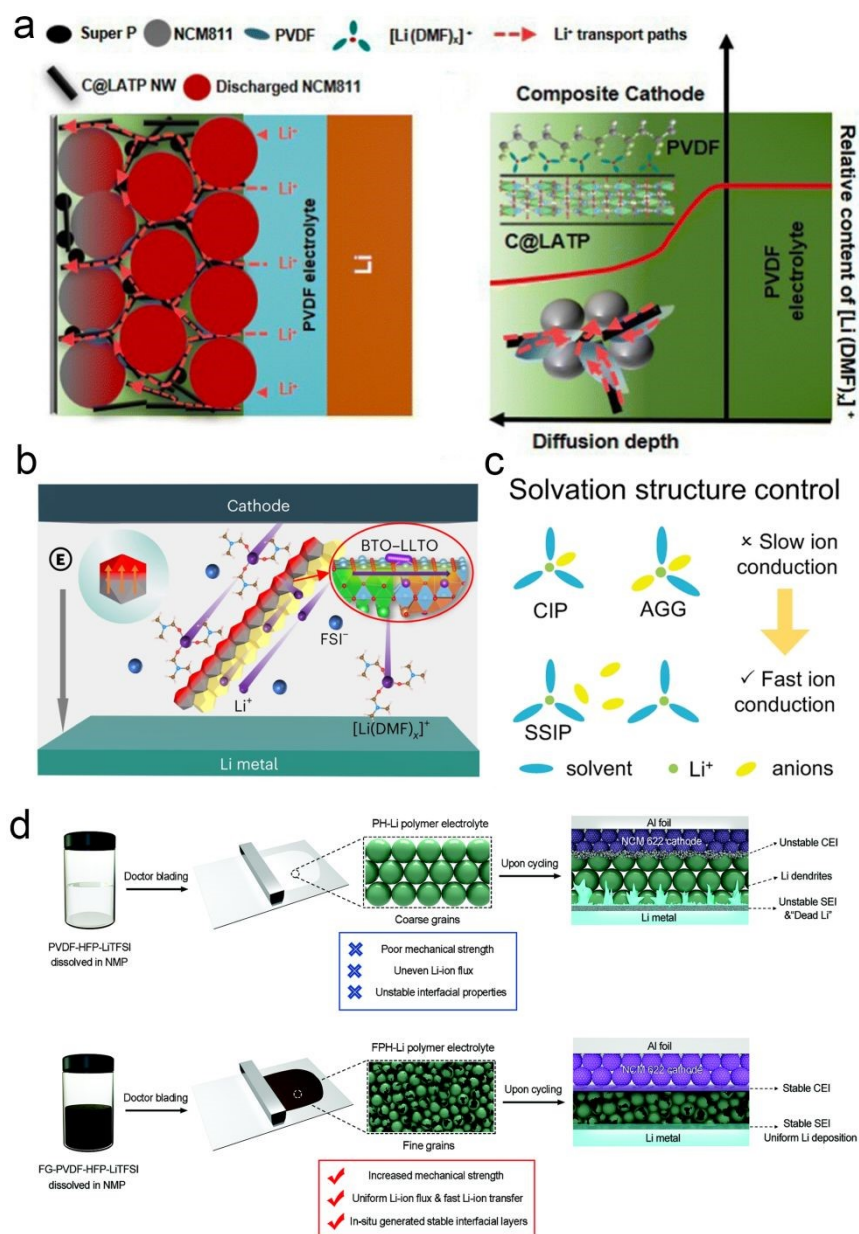


Fig. 10 Inorganic fillers anchor solvents to promote lithium salt coordination. a) Physical property of C@LATP NW filler and PCL-NCM cathode. Schematic of multiple Li^+ transport channels and diffusion of $[\text{Li}(\text{DMF})_x]^+$ in composite cathode with C@LATP NW. Reproduced with permission from ref. [116]. Copyright 2024, Royal Society of Chemistry. b) Illustration of the Li salt dissociation and Li^+ transport by the coupled BTO-LLTO in the PVBL electrolyte. Reproduced with permission from ref. [67]. Copyright 2023, Spring Nature. c) Solvation structure control. Reproduced with permission from ref. [68]. Copyright 2023, Spring Nature. d) Schematic illustration for the influence of fluorinated graphene on the properties of polymer electrolytes: Synthesizing process of common PVDF-HFP-LiTFSI (PH-Li) polymer electrolyte and the influence



of its inherent shortcomings on full-cell cycling. Synthesizing process of fluorinated-graphene reinforced PVDF-HFP-LiTFSI (FPH-Li) polymer electrolyte and the mechanism of its advantages for improving the cycling stability of the full-cell cell. Reproduced with permission from ref.[117]. Copyright 2020, Wiley-VCH GmbH.

4 Electrode-electrolyte interfaces

In recent years, the emergence of solid electrolytes has fundamentally solved the safety hazards of traditional liquid lithium-ion batteries, and is expected to achieve high energy density. However, due to the lack of fluidity of solid electrolyte, resulting in a series of problems such as small solid-solid contact area and increased impedance, these interface problems have become the bottleneck restricting the development of solid-state batteries. As shown in Fig. 11, the solid electrolyte interface mainly faces the following problems: interface electron/ion transport is poor, interface side reactions generate high impedance phase, stress powder occurs and dendritic growth.

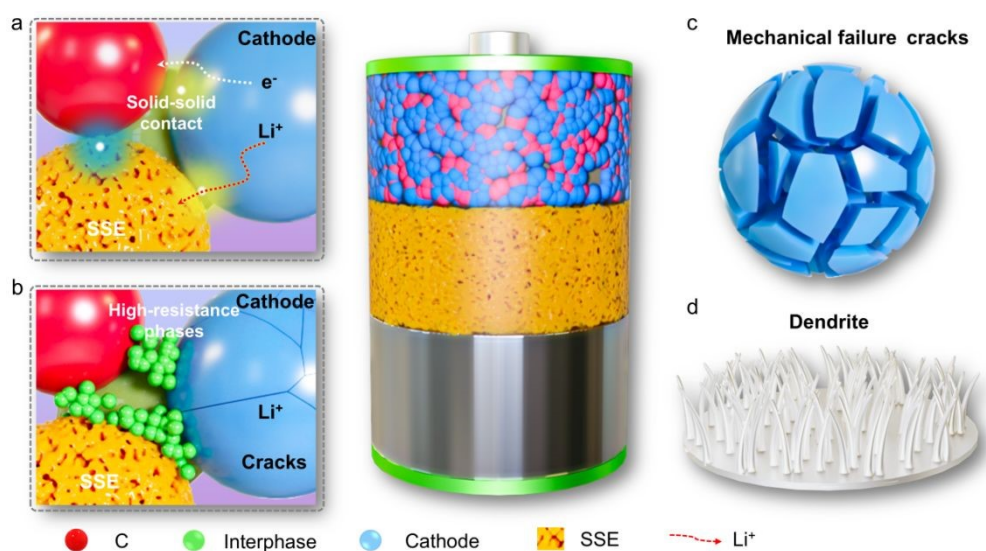


Fig. 11 Schematic diagram of solid electrode - electrolyte interface problems.

Compared with traditional liquid electrolytes, solid electrolytes do not have fluidity, so it is difficult to penetrate into the interface of the entire electrode and diaphragm, making ion/electron transmission slow at the interface, affecting the charge and discharge rate[118]. At the same time, the undesirable electron transport at the electrode/electrolyte interface can also induce chemical side reactions to form passivation mesophase leading to high interface resistance[119], which is a key factor affecting the electrochemical performance of solid-state batteries. Besides, during the



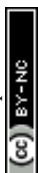
electrochemical cycling of the battery, the volume changes of the electrodes that occur during repeated charging and discharging cause a loss of interface contact, and also increase the interface impedance. And in ASSBs, the physical and mechanical stability of the solid electrolyte and electrodes isn't great, which can lead to structural stress at the electrode/electrolyte interface. As the electrochemical cycles continue, this structural stress keeps building up, and even occurs stress powder, ultimately affecting the battery's electrochemical performance. In addition, under working conditions, the charge and discharge rates as well as the operating voltage are key factors affecting the electrochemical stability of the interface. High charge and discharge rates can induce the formation of lithium dendrites on the lithium anode during the deposition and dissolution process[120], which can lead to battery short circuits and reduce the electrochemical performance of the battery.

In summary, the solid-solid interface problem is the main reason for the poor electrochemical performance of solid-state batteries. At present, the research on the interface of solid-state batteries has also achieved remarkable results, and this review summarizes the relevant results from the electrolyte and the contact of the positive electrode and the negative electrode respectively.

4.1 Electrolyte-cathode interface

4.1.1 Liquid, sulfide, oxide and polymer electrolytes with cathode interfaces

In conventional Li-ion batteries based on liquid electrolytes, the positive electrode particles can be completely submerged in the liquid electrolyte and may form a solid electrolyte interphase (SEI) passivation layer[121]. Therefore, good contact between the electrode and the liquid electrolyte can be maintained throughout the battery cycle. However, maintaining a tight electrode-electrolyte interface in solid-state lithium batteries is challenging, especially over multiple cycles. Poor contact in solid-state lithium batteries is likely to result in low active particle utilization, high polarization and even contact loss during cycling. There are significant differences in the contact behavior between various electrolytes due to different mechanical properties. Solid electrolytes are generally classified into SPEs and solid inorganic electrolytes, the latter



of which can be further classified into solid oxide and solid sulfide electrolytes. Due to the elasticity and deformability of organic polymers, polymer electrolytes have moderate contact with the positive electrode. However, cavities are still created due to interfacial reactions and crushing of the anode during cycling. As a result, the effective contact area between the anode and the polymer electrolyte will decrease as the cell cycles. Due to reasonable mechanical ductility, deformable sulfide particles can also change their shape to match the anode particles. Thus, poor contact between the electrode and the sulfide electrolyte can be greatly improved by mechanical compression. In contrast, contact loss can also occur as the anode particles shrink and expand during cycling. The point contact between the solid oxide electrolyte and the positive electrode is the poorest due to the rigid ceramic properties. Insufficient mechanical contact favors complete isolation of the cathode particles from the solid electrolyte, i.e., the "dead zone". Due to the lack of permeation pathways, neither electrons nor Li^+ can be transferred from or to the dead zone. The "dead zone" not only leads to direct capacity degradation, but also causes strong localized inhomogeneous current and strain distributions. Poor solid-solid contact usually leads to large polarization and low capacity. To improve the interfacial contact, various strategies have been adopted, such as in-situ synthesis of solid electrolytes, interfacial buffer layers, cathode coatings, and gel systems.

4.1.2 LiF-rich interface from liquid to solid electrolytes

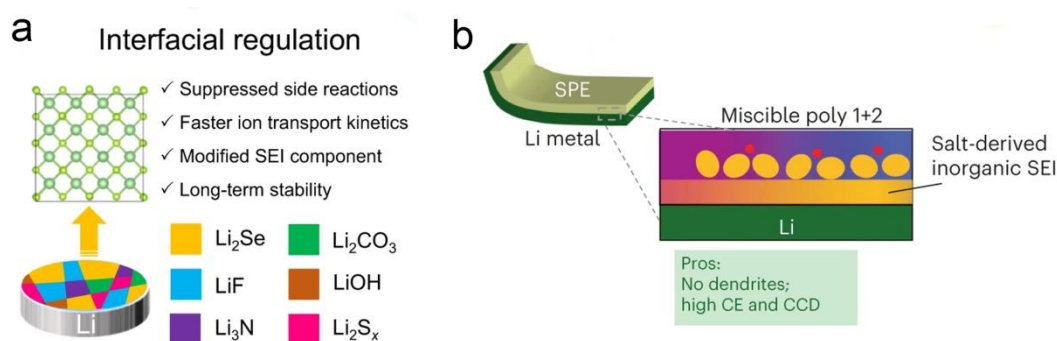
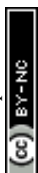


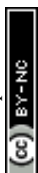
Fig. 12 Derived LiF-rich interface: a) interfacial regulation. Reproduced with permission from ref. [67]. Copyright 2023, Spring Nature. b) single-phase LPIFD. Reproduced with permission from ref. [109]. Copyright 2024, Spring Nature.

In recent years, with the development of new lithium-rich layered crystal



structures, the capacity of lithium-rich layered oxide anode materials (LLOs) can even reach an extremely high capacity of over 400 mAh g⁻¹. However, in addition to their amazingly high capacity, LLOs still suffer from low coulombic efficiency, poor multiplicative performance, and serious voltage degradation, which hinder their industrialization. Notably, for LLOs, a long plateau occurs during the first charging process above 4.5 V, which is believed to be the "activation" of the Li₂MnO₃ prototype framework, inducing irreversible oxygen release, void generation, and transition metal (TM) migration and phase transition. It is shown that oxygen release and transition metal ion migration start from the LLOs surface and extend to the bulk phase as the cycle progresses. In addition, side reactions between the anodically released O₂ and the electrolyte led to the formation of cathode electrolyte interphase (CEI). During the ensuing cycle, irreversible phase transition and CEI degradation continue to occur, leading to severe capacity loss, polarization growth and voltage decay.

Fluorinated electrolyte-induced F-rich CEI has been shown to improve the cycling stability of various cathode materials including LLOs, NCM811, etc. However, the high cost of fluorinated electrolytes will hinder the promotion of this strategy to some extent. Based on the basic idea of LiF-rich CEI strategy, fluoride-rich interfacial modulation is another feasible and effective method to achieve CEI modulation in LLOs. Wu et al.[111] designed a PVDF-based composite electrolyte with adding MoSe₂ sheets. The in-situ reactions between MoSe₂ and Li metal generate a Li-conducting Li₂Se component in SEI, which could suppress the DMF decomposition, improve the coulombic efficiency and enhance the interfacial ion transport kinetics (Fig. 12a). Wang et al.[109] designed the LPIFD electrolyte formed by combining two miscible polymers: Li-polymer (polymer-in-salt) and F diluter (inert fluorinated polymer) (Fig. 12b). The Li-polymer (polymer-in-salt) ensures continuous Li-ion conduction channels and contributes to the SEI, while the F diluter (inert fluorinated polymer) adds mechanical strength. Studies reveal that the single-phase LPIFD, which is based on a miscible polymer blend, lacks phase boundaries and forms an organic-less and LiF-rich SEI, effectively suppressing lithium dendrites. Lu et al. designed an artificially enhanced



CEI, with the main idea being to reduce the irreversible oxygen release and improve the stability of the material surface by constructing a high-pressure stable spinel combined with the introduction of a strong M-F bond[122]. More importantly, the F-rich structure on the material surface is beneficial for inducing the uniform deposition of LiF, which is conducive to the improvement of the lithium-ion transport properties. In addition, the strong polarity of F substitution facilitates the formation of a stable CEI layer. Compared with the conventional fluorine doping modification, the gradient doping method they developed avoids the conductivity drop and capacity loss caused by deep doping.

4.2 Electrolyte-anode interface

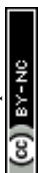
Heiskanen et al. proposed a mechanism for the evolution of SEI[123]. Initially, SEI were mainly composed of lithium ethylene decarbonate (LEDC) and LiF. However, LEDC is unstable and decomposes to produce a complex mixture of products. Since some of these components are soluble in electrolytes or gases, the remaining insoluble SEI becomes more porous. In addition, the remaining insoluble components are mainly inorganic: LiF, Li_2CO_3 and Li_2O . The remaining insoluble components become internal, more inorganic SEIs. At the same time, as the SEI becomes more porous, the electrolyte can reach the surface of the graphite electrodes, leading to further reduction of the electrolyte, generating additional LEDC and LiF. The new electrolyte reduction reaction results in the generation of external SEIs. In terms of composition and structure, most SEI films have a "mosaic" structure, consisting of disordered inorganic salts (such as lithium carbonate (Li_2CO_3), LiF) and organic substances (such as LEDC). It has also been shown that the electrochemical performance of batteries can be improved under certain conditions by modulating the interface to form a SEI film with a multilayer structure. The inner layer of this kind of electrode/electrolyte interface membrane is mainly inorganic materials such as LiF, Li_2CO_3 and Li_2O , which has a dense and compact structure with good thermodynamic stability, but it is easy to cause a significant increase in the interfacial impedance [124]. The outer layer is mainly organic materials such as lithium alkoxide (ROLi) and LEDC, which have loose and porous



structure and relatively poor thermodynamic stability. Therefore, the nature of the electrode/electrolyte interfacial film greatly affects the electrochemical performance of LIBs. The structure of the electrolyte not only determines the ion transport mechanism and the basic electrochemical properties of the electrolyte (conductivity, Li^+ transfer number), but can also affect the compatibility of the electrolyte with the electrode.

4.2.1 Graphite anode

Graphite, as an anode for commercial lithium-ion batteries, has a low and flat working potential, is structurally stable, low cost and environmentally friendly[125], and stable cycling in EC-based liquid electrolytes[126]. The graphite can be used as an anode in commercial Li-ion batteries. However, EC solvents have a high melting point (36.4 °C)[127] and poor oxidative stability (<4.3 V vs Li^+/Li)[128]. However, the high melting point (36.4 °C) and poor oxidative stability (<4.3 V vs Li^+/Li) of EC solvents limit the application of EC-based electrolytes in lithium-ion batteries[129]. The PC, as a lithium-ion battery electrolyte solvent, has a low melting point (−48.8 °C), good oxidative stability and strong lithium salt dissociation ability[130]. Therefore, PC-based electrolyte can be suitable for cathode materials with high energy density and operating voltage such as high nickel, and also has good performance at low temperature. However, when PC-based electrolytes are applied to graphite anode, the graphite structure will be damaged[126]. However, the application of PC-based electrolytes on graphite anode can cause damage to the graphite structure. The most widely accepted explanation for the incompatibility between PC-based electrolytes and graphite anodes is that in PC-based electrolytes, the solvent PC will be co-embedded with lithium ions in the graphite layer, and the co-embedded PC- Li^+ will undergo reductive decomposition, generating a large amount of propylene gas, which will strip off the graphite structure[131]. The solvent PC will be co-embedded with lithium ions in the graphite layer. Weakly soluble electrolytes based on carboxylate solvents have shown promise in overcoming the Li^+ de-solvation barrier for low-temperature battery operation[132]. It is found that in the organic anion-rich primary solvent sheath (PSS), the electrolyte tends to form a highly swollen and unstable SEI with high permeability



to the electrolyte components, which leads to a rapid degradation of the electrochemical performance of the graphite-based anode. Here, they proposed a facile strategy to regulate the swelling property of SEI by introducing inorganic anions into PSS via LiDfP co-solvation. By forming a low swelling SEI enriched with Li_3PO_4 , the parasitic reaction and solvent co-doping at the graphite-electrolyte interface that consumes the electrolyte are suppressed, which contributes to efficient Li^+ transport, reversible Li^+ (de)doping, and stable structural evolution of the graphite anode in high-energy lithium-ion batteries at low temperatures as low as $-20\text{ }^\circ\text{C}$ (Fig. 13a, b).

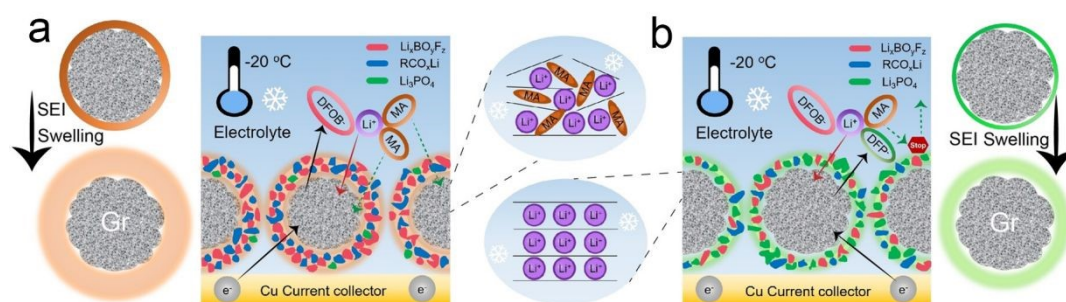


Fig. 13 Schematic illustrations showing the SEI swelling behavior and solvent co-intercalation mechanism of Gr anode for Pristine(a) and LiDfP-modified systems at $-20\text{ }^\circ\text{C}$ (b). Reproduced with permission from ref. [132]. Copyright 2023, Wiley-VCH GmbH.

4.2.2 Lithium metal anode

Lithium metal has the advantages of high theoretical specific capacity (3860 mAh g^{-1}), low electrochemical potential (-3.04 V vs. standard hydrogen electrode) and light weight ($\rho=0.53\text{ g cm}^{-3}$), so the use of lithium metal as the negative electrode of the battery can effectively improve the energy density of the battery[133]. The use of lithium metal as the negative electrode of the battery can effectively increase the energy density of the battery. When matched with a suitable cathode, the energy density of Li-metal batteries can reach $900\text{--}1900\text{ Wh L}^{-1}$ / $400\text{--}1000\text{ Wh kg}^{-1}$ [134]. However, Li-metal is highly reactive and thermodynamically unstable, and is prone to reacting with the electrolyte to form SEI. The SEI generated by the commercial carbonate electrolyte on the surface of Li-metal are usually heterogeneous and loose, which cannot protect the Li-metal electrodes and the electrolyte effectively. In addition, during the charging and discharging process, the volume of lithium metal changes greatly, mechanical stress will lead to the electrode and the electrode surface of the SEI broken, lithium uneven



deposition and dissolution on the surface of lithium metal, the formation of lithium dendrites. The continuous growth of lithium dendrites can lead to short circuit, triggering thermal runaway or even explosion of the battery. The rapid and uneven dissolution of lithium dendrites will cause lithium dendrites to separate from lithium metal, resulting in "dead lithium"[134].

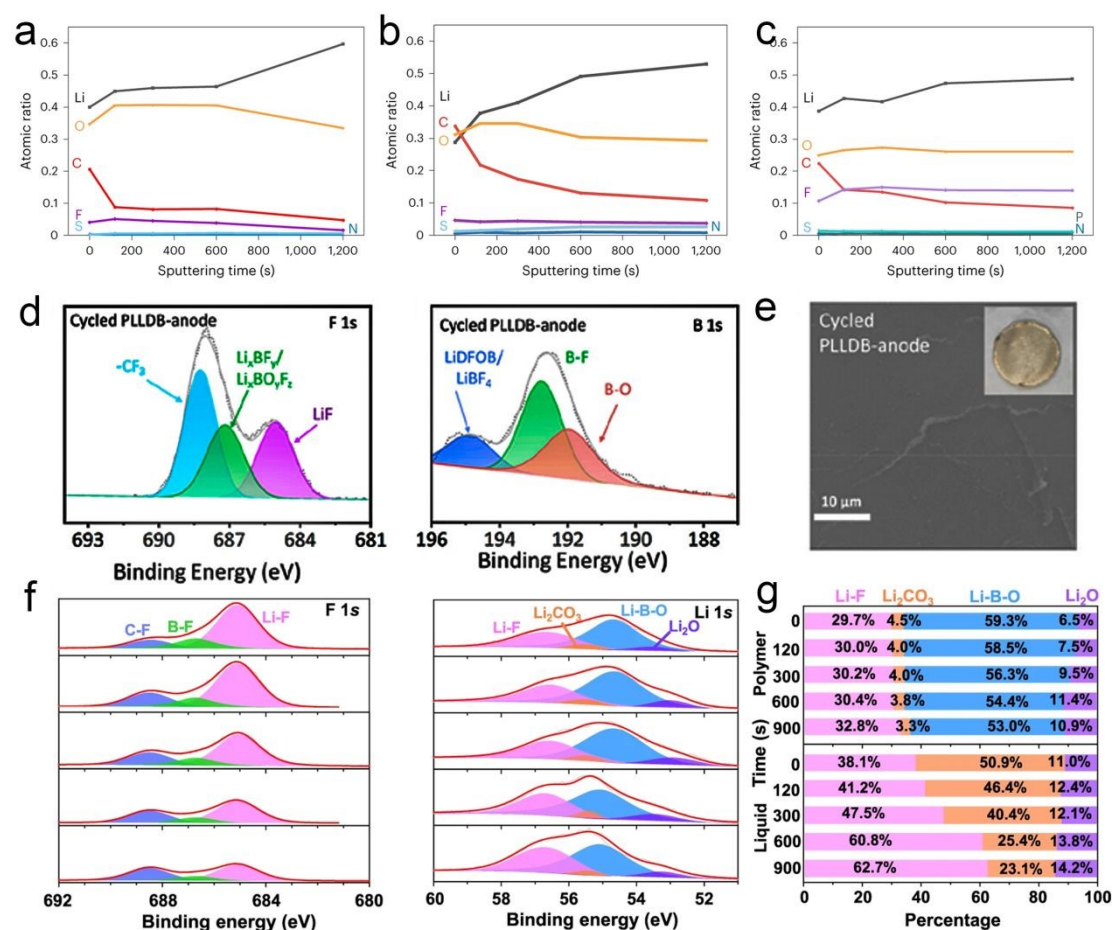


Fig. 14 SEI composition of polymer electrolyte with lithium anode. a-c) Quantified atomic composition ratios of the SEI at different sputtering times (0, 120, 300, 600 and 1,200 s from top to bottom) for PEO-LPIFD (a), PMMA-LPIFD (b) and PTFEP-LPIFD (c). Reproduced with permission from ref. [109]. Copyright 2024, Spring Nature. d) XPS spectra of F 1s and B 1s of the PLLDB-anode. e) SEM images of the surface morphologies of cycled Li metal anode disassembled from PLLDB. Reproduced with permission from ref. [135]. Copyright 2023, American Chemical Society. LMAs cycled in Li||Li coin cells with the designed polymer electrolyte: f) XPS depth profiles of F 1s and Li 1s, g) Relative compositions of Li-containing species. Reproduced with permission from ref. [136]. Copyright 2023, Spring Nature.

To solve these problems, Wang's team proposed a new electrolyte based on a polymer blend—LPIFD[109]. They performed XPS analysis of the SEI on the surface of the recycled Li anode for three LPIFDs, as shown in the Fig. 16a-c. LPIFD promoted



the formation of inorganic SEI due to the presence of high concentration of LiF in the SEI salt. Compared to the SEI observed in PEO-LPIFD with a significantly reduced carbon ratio (Fig. 14a) and the organic-rich SEI in PMMA-LPIFD (Fig. 14b), the atomic ratio of different elements of SEI in PTFEP-LPIFD remained almost constant from surface to inner layer (Fig. 14c). In the PTFEP-LPIFD system, the LiF-rich and uniform SEI structure is the result of the homogeneous distribution of PTFEP in PVDF-HFP. There is a significant repulsion between LiF and Li metal, resulting in a weak binding force and a high interfacial energy. This characteristic allows the SEI to bear less stress during the process of Li plating and stripping, thus maintaining good mechanical strength. In addition, sufficient LiF also promoted the lateral deposition of Li metal and inhibited the formation of Li dendrites. Therefore, the uniform and LiF-rich inorganic SEI in PTFEP-LPIFD plays a key role in preventing the formation of Li dendrites. In general, the inorganic-abundant interphases with a large electrochemical window and high Young's modulus can inhibit electrolyte decomposition and dendrite formation. Wang et al.[135] evaluated the interfacial composition of recycled batteries by XPS analysis. Significant LiF signals and $\text{LiB}_x\text{O}_y\text{F}_z/\text{Li}_x\text{BF}_y$ were observed on the PLLDB-anode (Fig. 14d). Combined with the results of the C1s spectroscopy, it can be inferred that a robust LiF-containing SEI layer is formed, which subsequently inhibits the decomposition of the electrolyte. In addition, SEM images of the cycled PLLDB-anode demonstrate the stability of SEI with the smooth and uniform morphology (Fig. 14e). Guo's team[136] also analyzed the SEI components formed in the electrolyte by XPS, as shown in Fig. 14f. In the case of the polymer electrolyte, it shows lower Li_2CO_3 intensity, and an additional signal of CF_3 can be detected. The existence of CF_x is further supported by the F 1s spectra, two other peaks at ~ 685 and ~ 686.8 eV, corresponding to LiF and B-F, respectively, suggest the preferred reactions of FDMA and DFOB^- with Li. According to the above results, the relative composition of lithium content substances at different depths is shown in Fig. 14g. In polymer systems, $\text{Li}_x\text{BO}_y\text{F}_z$ and LiF substances dominate SEI chemistry. With the increase of sputtering depth, the content of $\text{Li}_x\text{BO}_y\text{F}_z$ decreases, while the content of LiF increases. Thus, SEI in the polymer

View Article Online
DOI: 10.1039/D4MH01869A



system can be basically attributed to $\text{Li}_x\text{BO}_y\text{F}_z$ in the outer layer and LiF in the inner layer.

4.2.3 Silicon anode

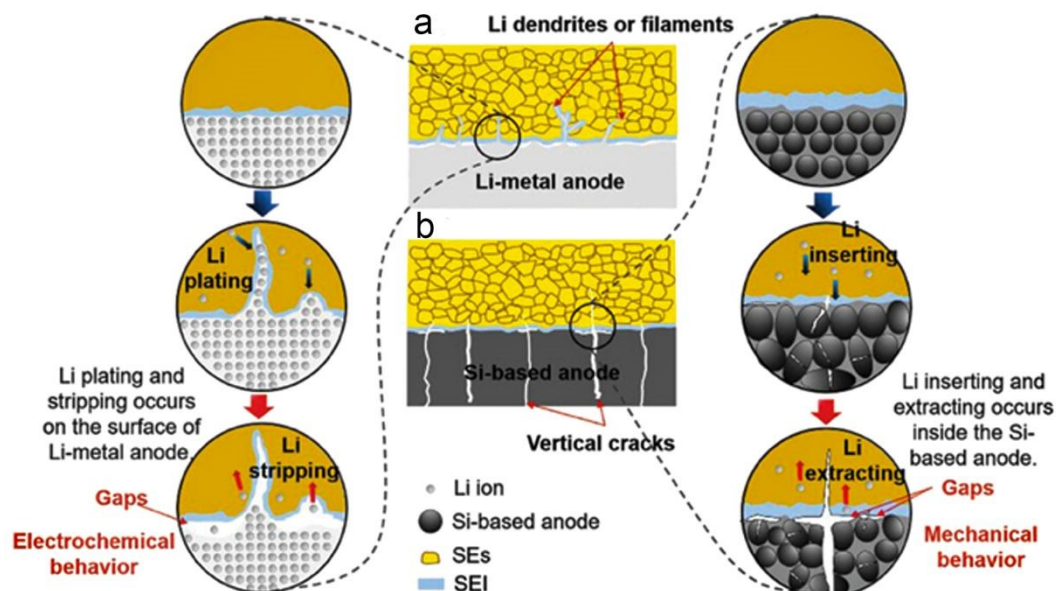
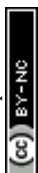


Fig. 15 Mechanisms of the interfacial gaps formed by a) Li-metal anodes and b) the Si-based anodes with the SEs, respectively. Reproduced with permission from ref. [137]. Copyright 2023, Wiley-VCH GmbH.

For lithium metal electrode, a large number of lithium ions are plated and stripped on the electrode surface, and these uneven deposits make the electrode surface form lithium dendrites, which can penetrate the electrolyte, causing a short circuit (Fig. 15a). Silicon is an attractive anode material for energy storage devices because it has a theoretical capacity 10 times that of its state-of-the-art carbon counterpart. Silicon anodes can be used both in conventional lithium-ion batteries and, more recently, in lithium-oxygen and lithium-ion batteries as an alternative to dendrite-formed lithium-metal anodes. For Si-based anodes (Fig. 15b), large amounts of Li-ions are inserted and extracted within the electrode, causing the structural degradation and instability of the solid electrolyte interphase due to large volume changes ($\sim 300\%$) during cycling, side reactions with the electrolyte, and low volume capacity when the material size is reduced to the 4–7 nm scale[138]. Compared to bulk silicon, nanostructured silicon typically has significantly shorter transport paths for both lithium ions and electrons, thus ensuring good multiplicative capacity. In addition, nanostructured silicon produces



less internal stress during Li^+ insertion and embedding reactions, ensuring stable volume change and high capacity[139].

As shown in Fig. 16a, Masuda et al. performed an in situ XPS experiment to characterize the SEI formation at the interface between the Si electrode and the LLZTO electrolyte during the first cycle with Li metal as the counter electrode[140]. The Li 1s peak in the XPS spectra shows several lithiation products consisting of Li_2O , Li_2CO_3 , Li_4SiO_4 and Li_xSi , and the same lithiation products are also demonstrated in the Si 2p and O 1s spectra. Notably, the presence of Li_2O and Li_2CO_3 suggests that trace oxygen species and carbon dioxide may be derived from the reaction products of the XPS chamber or LLZTO with the lithium silicide surface. In general, the small number of interfacial products and the high coulombic efficiency of the half-cell indicate that the side reactions at the interface between the Si anode and the LLZTO electrolyte are suppressed. Our team proposed a $\text{Si}@\text{SiO}_2@\text{LPO}@\text{C}$ composite negative electrode and applied it to a liquid electrolyte and a PEO/LATP ASSE, respectively[141]. The TEM images in Fig. 16b show the cycling silicon composite particles and the SEI layer of the disassembled ASSB after 200 cycles. Notably, conformal particles and uniform SEI layers were observed from the ASSB, and the LiTFSI in the ASSE contributed to the formation of LiF nanocrystal-rich SEI layers with mechanical robustness and high ionic conductivity. For PEO-LiTFSI solid electrolytes, LiTFSI is preferentially reduced over PEO, and thus the decomposition of LiTFSI to produce LiF is thermodynamically favorable.

View Article Online
DOI: 10.1039/D4MH01869A



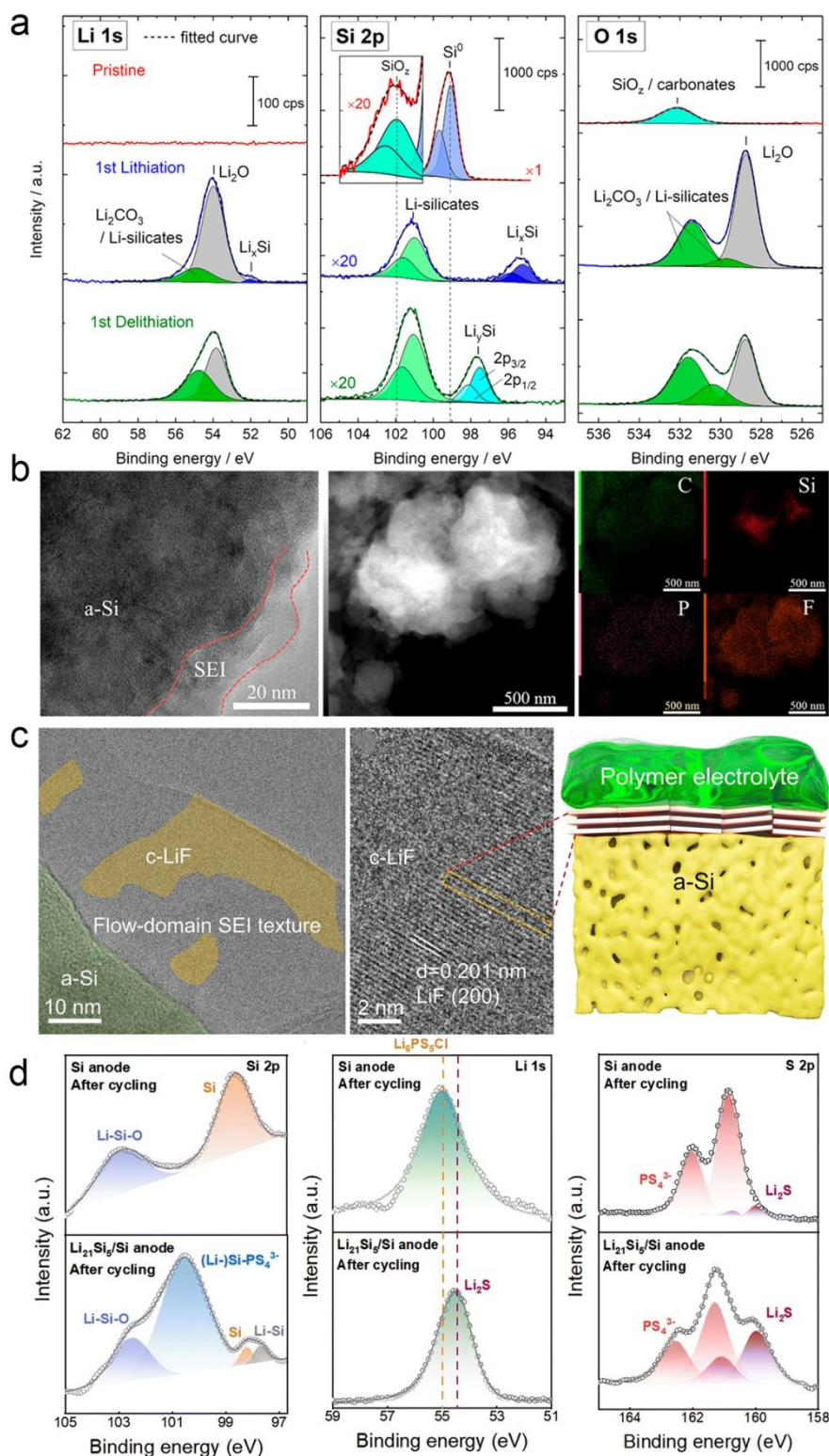


Fig. 16 SEI components deposited on Si anode surface. a) Li 1 s, Si 2p, and O 1 s spectra of the Si electrode at different states: pristine state, after the first lithiation, and after the first delithiation process. Reproduced with permission from ref. [140]. Copyright 2020, American Chemical Society. b) TEM images, HADDF-STEM images, and the corresponding elemental distributions of $\text{Si}@\text{SiO}_2@\text{LPO}@\text{C}$ composite anode after 200 cycles from the ASSB. Reproduced with permission from ref. [141]. Copyright 2022, Elsevier. c) Cyro-TEM and high-resolution TEM

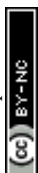
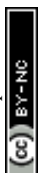


image of the surface SEI on the PS-Ag-C electrode after 500 cycles. The schematic diagram of the SEI formed on the surface of cycled PS-Ag-C in a solid-state cell. Reproduced with permission from ref. [142]. Copyright 2023, Royal Society of Chemistry. d) XPS tests of Si-ASSBs and Si/Li₂₁Si₅-ASSBs after 50 cycles. Reproduced with permission from ref. [144]. Copyright 2024, Royal Society of Chemistry.

Besides, our team propose a design of highly dense Ag nanoparticles decorated with porous micro sized Si, which is coated by thin-layer carbon (PS-Ag-C) working as a high-performance anode for boosting SSB performance[142]. As shown in Fig. 16c, a large amount of LiF on the electrode surface was observed in the SEI region by cryo-TEM. It was observed that the LiF particles showed a well-oriented flow-domain like pattern, which are parallel with the surface of PS. Then, Zhang' team developed a Si/Li₂₁Si₅ composite anode with the rational architecture and optimized ratio of Li₂₁Si₅ and pure Si[144]. They disassembled the cells after the cycle and analyzed the role of the Li₂₁Si₅ alloy in the anode. Fig. 16d shows the results of its XPS and cross-section SEM characterizations. After adding the Li₂₁Si₅ alloy, (Li-) Si-PS₄³⁻ (100.5 eV) and Li-Si (97.6 eV) were found on the surface of the anode, indicating that Li₂₁Si₅ alloy can continue to provide efficient ion/electron conductive channels and stable lithium supply, making the electrochemical reaction of SSBs more complete. This is further supported by the addition of Li₂S in the Li 1s and S 2p orbitals. As an electronic insulator, Li₂S can prevent further decomposition of Li₆PS₅Cl in time to build a stable SEI. Therefore, an efficient transmission channel is successfully constructed inside the anode.

4.3 Advanced characterization techniques on lithium-ion transportation and interphases

In SSEs, information about the transport of lithium ions and the interface can be obtained through a variety of characterization techniques, Fig. 17 illustrates some of these characterization techniques, including two-dimensional nuclear magnetic resonance spectroscopy (2D NMR), cryogenic transmission electron microscope (cryo-TEM), Raman spectrum and nano infrared spectrum (Nano-IR).



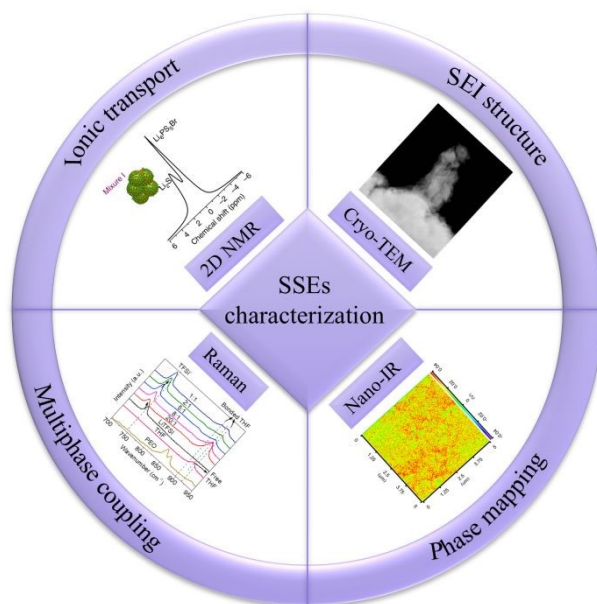


Fig. 17 Schematic diagram of SSEs characterization

4.3.1 2D NMR

NMR is a useful tool for exploring ion transport in electrode materials during electrochemical cycling. Most NMR studies of lithium-ion battery materials are performed ex situ: the cell is cycled to a specific state of charge, the sample is split and extracted, and then NMR is performed on that sample. In situ NMR provides a simple means to study the conditions under which dendrites form and to monitor their growth. Wang et al.[145] used 2D ${}^7\text{Li}$ - ${}^7\text{Li}$ exchange NMR to study the local exchange kinetics between Li^+ (-0.91 ppm) coordinated to PEO chain segments and Li^+ (-0.78 ppm) coordinated to PEO chain ends. Fig. 18a shows 2D ${}^7\text{Li}$ - ${}^7\text{Li}$ obtained using exchange times ranging from 1 to 200 ms exchange spectra. The experimental temperature was 305 K. Significant cross peaks were observed in the spectra, indicating the existence of exchange kinetics between the two Li^+ substances. Yu et al.[48] used two-dimensional exchange NMR spectroscopy (2D-EXSY) to provide unique quantitative insights into spontaneous exchange between solid electrolytes and electrodes. Using differences in NMR chemical shifts, lithium-ion transport at the interface of Li_6PS_5 Br- Li_2S anode mixtures was measured at different stages of the preparation process as well as before and after cycling, providing unprecedented insights into the evolution of the electrical resistance between the solid electrolyte and the anode. The size of the nano Li_2S and



the intimate contact with the silver pyroxene $\text{Li}_6\text{PS}_5\text{Br}$ electrolyte are necessary to provide measurable charge transfer at the interface. The 2D NMR spectra shown in Fig. 18b-g indicate a broad-spectrum homogeneous resonance for ^7Li in Li_2S , and a star resonance for ^7Li in $\text{Li}_6\text{PS}_5\text{Br}$. The latter is a result of the high mobility of lithium ions in the solid electrolyte of $\text{Li}_6\text{PS}_5\text{Br}$, which leads to a Lorentzian line shape, and after 2D Fourier transform, a star-shaped NMR is observed.

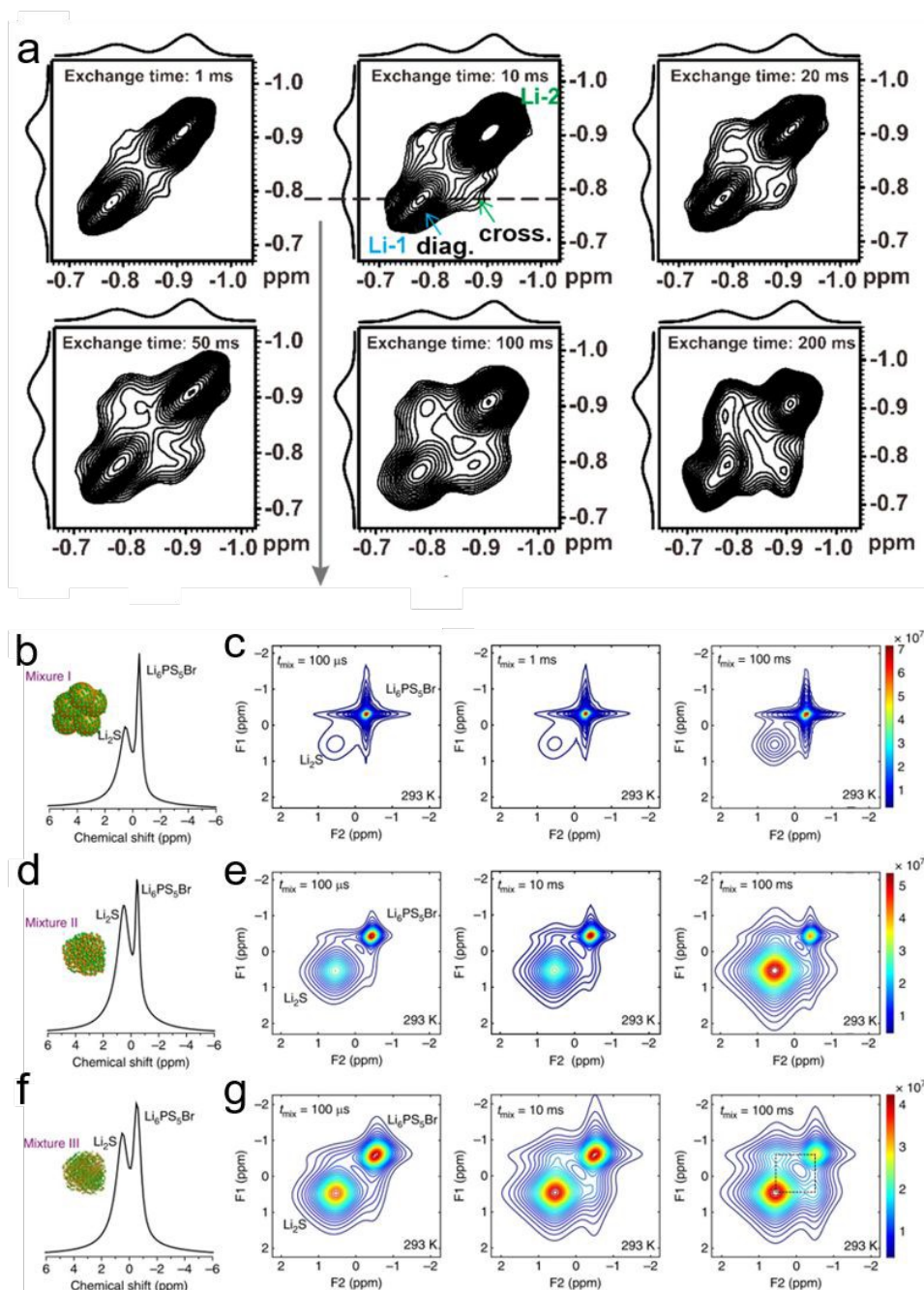
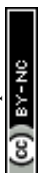


Fig. 18 a) The 2D ^7Li - ^7Li exchange spectrum of IM240-PEO/ Li^+ . This spectrum was acquired using an exchange time of 1 to 200 ms at 305 K. Reproduced with permission from ref. [145]. Copyright 2020, MDPI. NMR measures the spontaneous lithium-ion transport between the $\text{Li}_6\text{PS}_5\text{Br}$ solid



electrolyte and the Li_2S cathode. b, d, f) One-dimensional (1D) ^7Li magic angle spinning (MAS) spectra corresponding to the $\text{Li}_6\text{PS}_5\text{Br-Li}_2\text{S}$ cathode mixtures a mixture I, where Li_2S is micron-sized e mixture II, where Li_2S is nanosized i mixture III, where nanosized Li_2S is thoroughly mixed with $\text{Li}_6\text{PS}_5\text{Br}$. c, e, g) Two-dimensional (2D) $^7\text{Li-}^7\text{Li}$ exchange spectra (2D -EXSY) recorded at a ^7Li resonance frequency of 155.506 MHz and a spinning speed of 20 kHz at RT for short (100 μs) to long mixing times t_{mix} (100 ms) for c mixture I, e for mixture II, and g for mixture III. Reproduced with permission from ref. [48]. Copyright 2017, Spring Nature.

4.3.2 Cryo-TEM

In order to fully understand the role of SEIs, lithium-based compounds need to be thoroughly studied and characterized. Their structure, composition, size, number, ionic conductivity, stage of formation and evolution are all of interest. Many factors affect SEI formation, including electrode potential, current density, number of cycles, type of negative electrode, electrolyte composition, and even temperature[146]. Cryo-TEM holds the promise of resolving the long-debated issue of SEI structure. In addition to the use of lithium metal anodes to achieve maximum energy density, the safety of lithium dendrite growth has also attracted attention, and the growth mechanism of lithium-ion dendrites can be observed on an atomic scale using cryo-TEM. Lin et al. used cryo-STEM to study the morphology and chemical composition of Li, as shown in Fig. 19, which were obtained by electroplating using baseline SN-bound PolyEA SPE (SNSPE) at 0.1 mA current for 60 min[147]. Fig. 20a-c show representative high-angle annular dark field STEM (HAADF-STEM) images of several Li filaments from different regions images. The results show that these filaments are morphologically different from those previously reported for liquid electrolyte systems, and the lithium filaments grown in liquid electrolytes appear to be dense Li_2O dendrites coated with SEI membranes. In HAADF-STEM or Z-contrast imaging modes, the internal contrast of these dendrites (corresponding to Li^0) is typically darker than that in SEI, however, in baseline SN-SPE, the lithium filaments show bright contrast in most regions, while only a few dark domains or streaks are observed (as indicated by the red arrows in Fig. 19a), which suggests that a side-reaction has occurred and that the cracks or voids have formed in the filaments. To investigate the three-dimensional (3D) internal structure of the filaments, cryo-STEM tomography was performed. 3D reconstruction (Fig. 19b)



and cross-sectional analysis (Fig. 19c) of a representative filament showed that multiple cracks were formed throughout the filament, which could be attributed to the large stresses caused by the volume change during the SN-SPE side reaction. Energy dispersive X-ray spectroscopy (EDS) maps (Fig. 19d and e) and electron energy loss spectroscopy (EELS) results (Fig. 19f) of several filaments showed that all examined filaments, regardless of their morphology and dimensions, contained significant amounts of oxygen, carbon, sulfur, fluorine, and nitrogen.

View Article Online
DOI: 10.1039/D4MH01869A



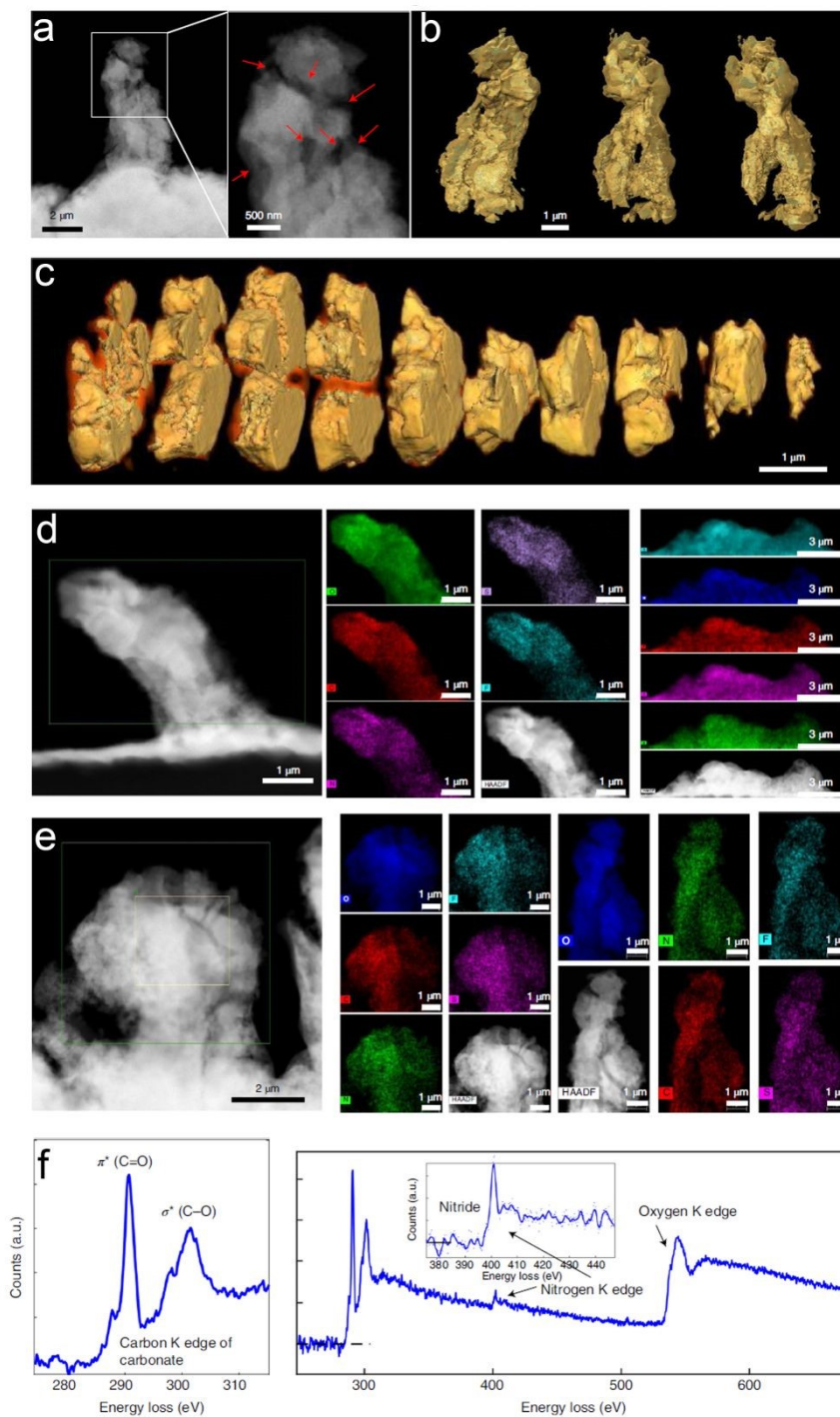


Fig. 19 3D morphology and chemistry of the Li-containing dendrites plated using the baseline succinonitrile-incorporated solid polymer electrolyte (SN-SPE). (a) and (d) Cryogenic annular dark-field scanning transmission electron microscopy (ADF-STEM) image and (b) 3D reconstruction of a representative filament obtained by cryogenic tomography based on ADF-STEM images. (c) 3D cross-section analyses of the filament in (a). (d) and (e) Energy-dispersive X-ray spectroscopy (EDS) maps of several filaments from different regions. The results show that O, C, N, S, and F are distributed throughout the whole filament in all regions. The results show that O, C, N, S, and F are distributed throughout the whole filament in all



locations. (f) Electron energy-loss spectroscopy (EELS) of the filament. C, N, and O species are identified in the spectra. Reproduced with permission from ref. [147]. Copyright 2022, Springer Nature. View Article Online
DOI: 10.1039/D4MH01869A

4.3.3 Raman spectrum

Raman spectrum has proved to be a powerful method for characterizing electrode materials for lithium-ion batteries, providing important multiphase coupling information, complementing XRD, and enabling microscopy and in situ/operando measurements. In addition, it is simple to apply and does not require specific sample preparation [148]. Chrissopoulou et al. [149] measured the Raman spectra of PEO and nanocomposites with different polymer concentrations, and they found that due to the crystalline phase of the polymer, the spectra of pure PEO as well as blends with high polymer content are dominated by sharp vibrational bands. Among them, the Raman spectra of blends with 65 wt.% and 30 wt.% PEO were significantly different, showing peak shifts (Fig. 20a). The bands appearing in these spectra are comparable to the Raman bands of the PEO melt, and in these cases the polymer is predominantly amorphous. Hu et al. developed a novel in-situ polymerization integrated ultrathin SE/anode design for Raman spectroscopy of PVC/SN-LLZTO, PVC/SN and PVC electrolytes in the range of 730–760 cm^{-1} (Fig. 20b), and the curved vibrational peaks of $-\text{CF}_3$ in TFSI^- can be deconvoluted into two peaks, referring to the unliganded free TFSI^- and liganded TFSI^- [150]. It can be seen that the percentage of free TFSI^- in PVC/SN-LLZTO CSEs is 40.8% while the percentage of free TFSI^- in PVC/SN electrolyte is 34.5%, both of which are higher than that of PVC electrolyte alone (only 15.9%). This result is mainly attributed to the high dielectric constant of SN ($\epsilon \approx 22$), which greatly facilitates the dissociation of lithium salts. In addition, the LLZTO filler with abundant surface Lewis's base sites also contributes to the dissociation of lithium salts via Lewis's acid-base interactions. Higher ratios of free TFSI^- usually indicate more Li salt dissociation as well as higher carrier concentrations. Liu et al. measured the Raman spectra of LATP NW and C@LATP NW (Fig. 20c), which showed that C@LATP NW displays D and G bands at 1358 and 1596 cm^{-1} , respectively, suggesting that an amorphous carbon layer about 5 nm thick was successfully coated on the LATP



surface[116].

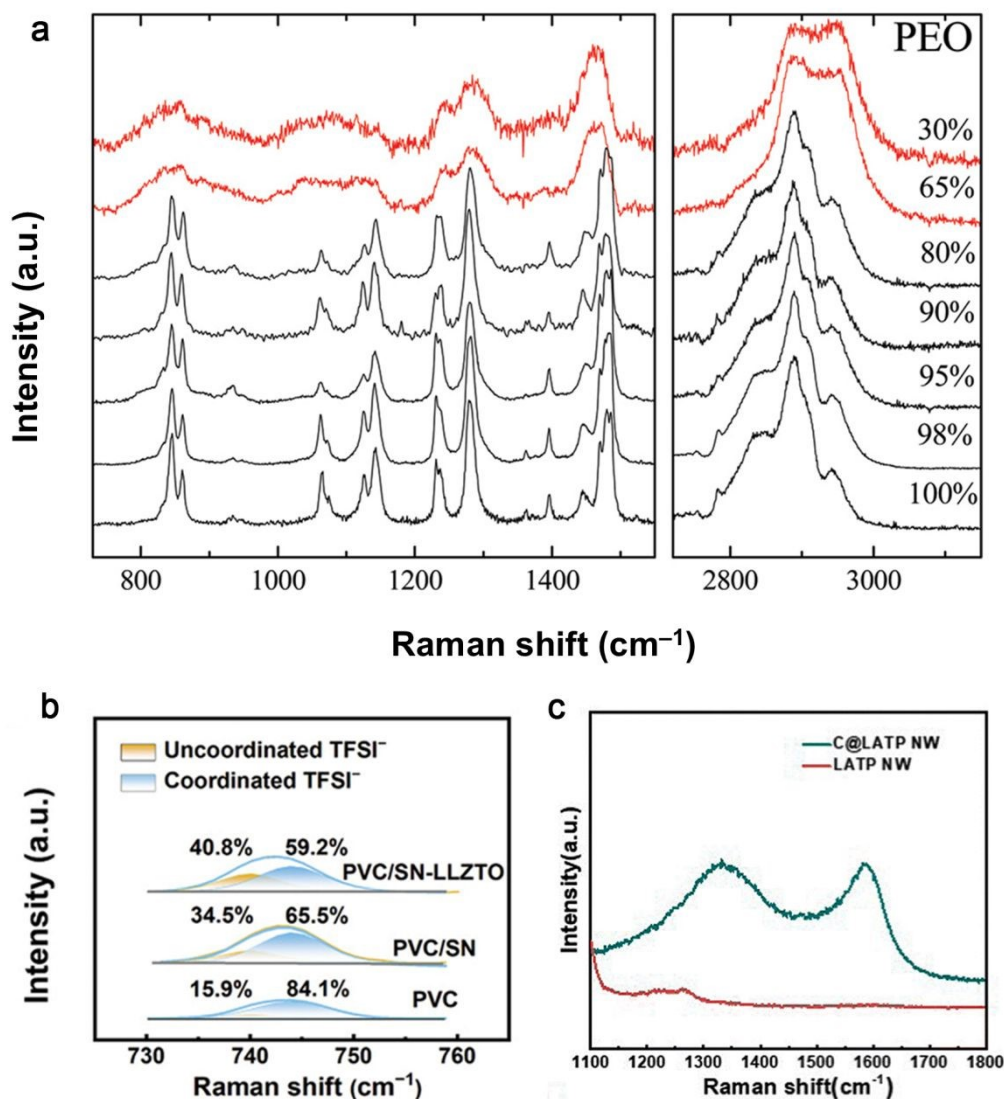


Fig. 20 Raman spectra of a) PEO and of PEO/Na⁺-MMT nanocomposites with different polymer concentrations at ambient temperature. Reproduced with permission from ref. [149]. Copyright 2011, American Chemical Society. b) PVC, PVC/SN and PVC/SN-LLZTO SEs in the range of 730–760 cm^{-1} . Reproduced with permission from ref. [150]. Copyright 2024, Wiley-VCH GmbH. c) the C@LATP NW and LATP NW. Reproduced with permission from ref. [116]. Copyright 2024, Royal Society of Chemistry.



4.3.4 Nano-IR

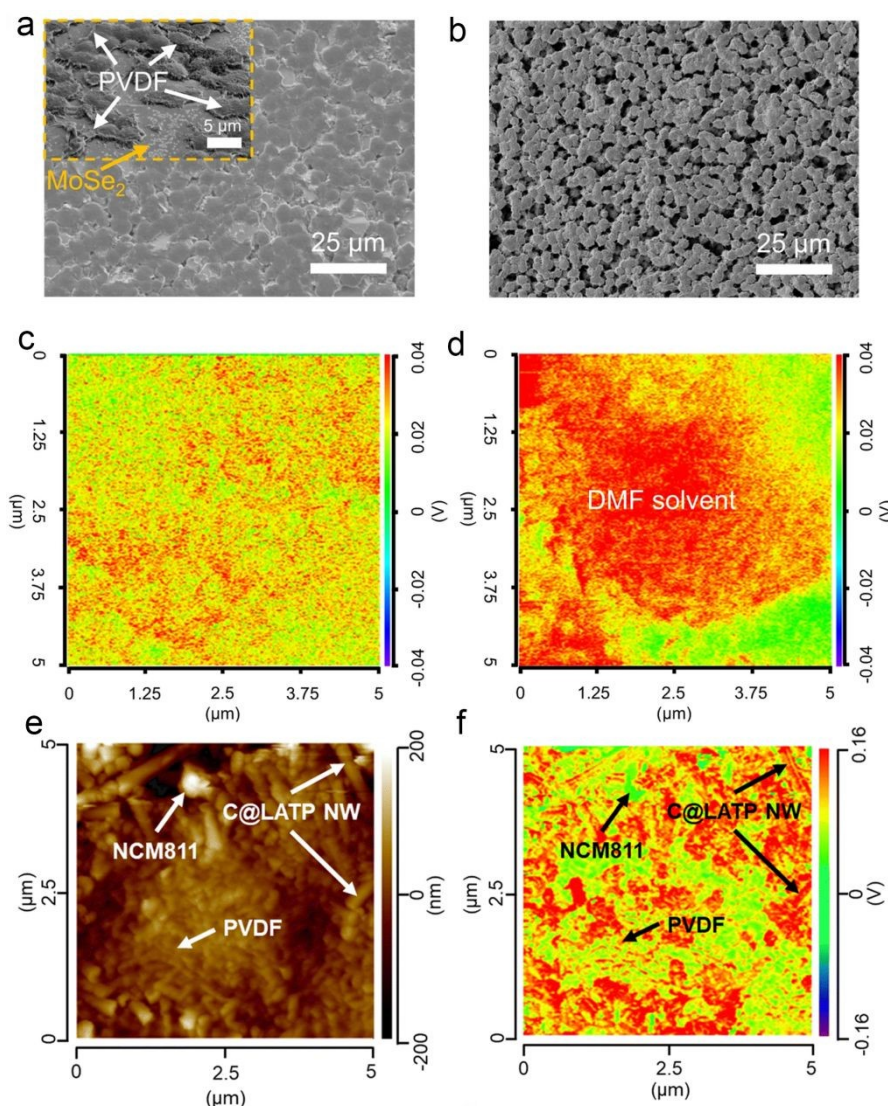
View Article Online
DOI: 10.1039/D4MH01869A

Fig. 21 a) Surface SEM image of the PVMS-15 electrolyte. The inset is surface of PVMS-15 electrolyte obtained from FIB-SEM. b) Surface SEM image of the PVDF electrolyte. Nano-IR overlap of the C=O vibration of DMF solvent in the PVMS-15 (c) and PVDF (d) electrolytes. The red color area means the existence of DMF solvent while the green color area means the absence of DMF solvent. solvent while the green color area means the absence of DMF solvent. Reproduced with permission from ref. [68]. Copyright 2023, Spring Nature. e) AFM image of the PCL-NCM cathode. f) Nano-IR overlap of the C=O vibration of DMF solvent at 1663.27 cm^{-1} . Reproduced with permission from ref. [116]. Copyright 2024, Royal Society of Chemistry.

Infrared (IR) spectroscopy has been used to probe the phase mapping of polymers and the physical interactions between components in SPEs. IR spectroscopy is very sensitive to the extent of hydrogen bonding. Wu et al. performed atomic force microscopy-nano-infrared spectroscopy (AFM-nano-IR) to detect C=O groups of DMF in PVMS-15 and PVDF electrolytes[67]. On the surface of the PVMS-15 electrolyte,



the intensity of the absorption peaks remained low and consistent (Fig. 21c), which favored the formation of a dense SEI and inhibited the decomposition of DMF. On the contrary, the DMF solvent aggregates around the PVDF spherical crystals (Fig. 21d), which always causes inhomogeneous lithium deposition and rapid lithium dendrite growth. Thus, the adsorption between MSs and PVDF not only produced a dense electrolyte, but also led to a uniform solvent distribution. Liu et al. The distribution of DMF in 3 wt.% C@LATP NW in PCL-NCM cathode was further examined by nano-IR (Fig. 21e, f)[116]. The strength of the C=O group was much stronger on C@LATP NW, suggesting that most of the DMFs were anchored to the surface of the high specific surface area C@LATP NW because of their higher adsorption energy.

5 Electrochemical performances

Solid state battery assembled by polymer-inorganic solid electrolyte not only has high ionic conductivity, wide electrochemical window, but also has good electrochemical performance, including high voltage cathode, high mass load, wide temperature range and low external pressure. Table 2 has summarized the relevant electrochemical properties of some polymer-inorganic SSBs. Through modification and structural design, the electrochemical performance of the electrolyte can be improved to enhance the energy density and cycle life of solid-state batteries.

Table 2 Summary of the electrochemical performance for polymer-inorganic SSBs.

Electrochemical performance	Polymer matrix	Li Li symmetrical cell cycle life	Cathode	Cathode voltage/ V	Full cell cycle life and capacity retention	Loading of cathode/ (mg cm ⁻²)	References
High voltage cathode	PEO-LLZTO	-	LiCoO ₂	4.5	0.2C 60°C 200cycles retaining 110.4 mAh g ⁻¹	1.5–2	[151]
	PEO-LLZNO	-	LFP	5.2	0.5C 60°C 150cycles 97% retention	2	[153]
	PEO-LLZTO	60°C 0.2mA cm ⁻² 400h	LFP	5.5	0.1C 60°C 100cycles 83% retention	4.7	[154]



View Article Online
DOI: 10.1039/D4MH01869A

	PEO-LLZTO	55°C 0.5mA cm ⁻² > 680h	LFP	5	0.2C 55°C 100cycles 98.6% retention	2-3	[155]
	PEO@ZIF-8	-	NCM811	4.9	0.2C 60°C 149.8mAh g ⁻¹ 2.8-4.3V 100cycles 83.2% retention	-	[152]
	PEGDME	0.2mA cm ⁻² 2500h	NMC532	4.3	0.2C 100cycles 97% retention	3-4	[156]
High loading capacity	PVC/SN-LLZTO	-	NCM811	4.96	0.1C RT 100cycles 72.4% retention	8.3	[150]
	PEO-PAN	-	NCM811	4.9	0.35mA cm ⁻² 50°C 100cycles 78% retention	23	[160]
	PEO-LLZTO	0.2mA cm ⁻² > 960h	LFP	4	0.1mA cm ⁻² 155.7mAh g ⁻¹	11	[157]
	PEGDA	25°C 0.5mA cm ⁻² 2000h	LFP	-	0.1C 25°C 55cycles 96.4%retention	16.43	[158]
	BPCT-PE	0.5mA cm ⁻² 500h	NCM811	4.3	0.2C 600cycles 70% retention	7.5	[159]
Wide temperature range	PPC/LLZTO	25°C 0.05mA 1000h	LFP	> 4	0-160°C 20°C 1C 800cycles 95% retention	-	[161]
	PEO/SiO ₂ - aerogel	0.05mA cm ⁻² 450 cycles	LFP	-	15-65°C 15°C 0.4C 105mAh g ⁻¹ 55°C 0.1mA cm ⁻² 25cycles	7.4-13.6	[162]
	PEG	-	LFP	-	80°C 3.8-4.2V	-	[164]
	PCL-PPC- PCL	70°C 0.1mA cm ⁻² 760h	LFP	5	70°C 0.1C 200cycles 90% retention	1.5	[165]



	PEO/SN	0.1 mA cm^{-2} 450h	LFP	4.2	0°C 0.1C 180cycles 97.3% retention	1	[166]
Low external pressure	Poly-AM	0.1 mA cm^{-2} 1800h	LFP	4.3	546 and 52kPa, 1C 400cycles 97.1% retention	6	[167]
pressure	PEO/PVDF	0.1 mA cm^{-2} > 1000h	LFP	-	RT 0.1C no external pressure 200cycles 98.5% retention	3	[168]

5.1 High voltage performance

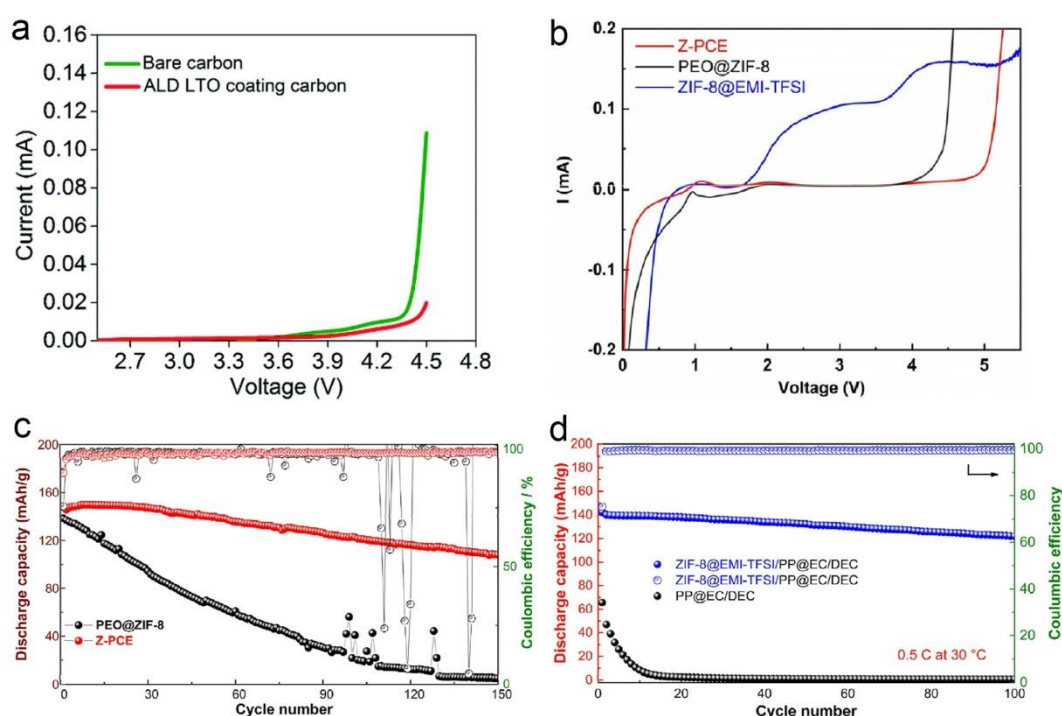


Fig. 22 a) Comparison of the linear sweep voltammogram of the Li/SPE/PEO-carbon composite cell and Li/SPE/PEO-LTO@carbon composite cell (scan rate = 0.3 mV s^{-1} , from OCV to 4.5 V vs. Li/Li^+). Reproduced with permission from ref. [151]. Copyright 2020, Royal Society of Chemistry. b) LSV of Z-PCE, ZIF-8@EMI-TFSI, PEO@ZIF-8 at 60 °C. c) Cycle performance of PEO@ZIF-8 and Z-PCE half cells at 0.2 C under 60 °C. d) Cycle performance of PEO@ZIF-8 and Z-PCE half cells at 0.5C under 30 °C. Reproduced with permission from ref. [152]. Copyright 2022, Elsevier.

To date, high voltage Li-Metal batteries have been severely limited due to electrolyte instability to Li-Metal negative electrodes and high voltage positive electrodes. The instability of PEO-based SPEs at high voltages has received little research attention. The instability of PEOs at high voltages makes coupling to high



voltage cathodes such as LiCoO_2 challenging. Sun et al.[151] chose atomic layer deposition (ALD) for the coating of active material particles and the entire electrode coating. In this study, ALD-derived lithium tantalate protective coatings were shown to stabilize the interface between PEO-based SPEs and LiCoO_2 electrodes at high voltages (4.5 V vs. Li/Li^+) (Fig. 22a). The effect of the coating on LiCoO_2 particles, the whole electrode and the conducting carbon particles were compared. The results showed that the coating on LiCoO_2 particles could not improve the performance of ASSLBs, while the coatings on the electrode sheet (LiCoO_2 particles and coatings on carbon particles) showed significant enhancement of cycling performance, same as the coatings on the conductive carbon particles. Shen et al.[152] prepared an ion-conducting asymmetric PEO-based electrolyte consisting of a zeolite imidazolium ester skeleton (ZIF-8) @ ionic liquid protective coating on the surface of the NCM811 positive electrode and a PEO-based electrolyte with ZIF-8 nanofillers on the lithium metal anode to construct high-performance solid-state lithium metal batteries. The prepared asymmetric composite electrolytes exhibited a high ionic conductivity of $9.02 \times 10^{-4} \text{ S cm}^{-1}$ at 60°C and a wide electrochemical stability window of more than 4.9 V (Fig. 22b). As shown in Fig. 22c-d, the prepared cell exhibited the highest discharge capacity of 150 mAh g^{-1} at 60°C , 0.2 C. It was found that the ZIF-8@ ionic liquid protective coating effectively prevented the oxidative decomposition of the PEO-based electrolyte and the dissolution of transition metals from the anode at high voltage. Meanwhile, the growth and penetration of lithium dendrites were also inhibited, which shows great potential for advancing the commercialization of high-voltage lithium-metal batteries.



5.2 High loading capacity

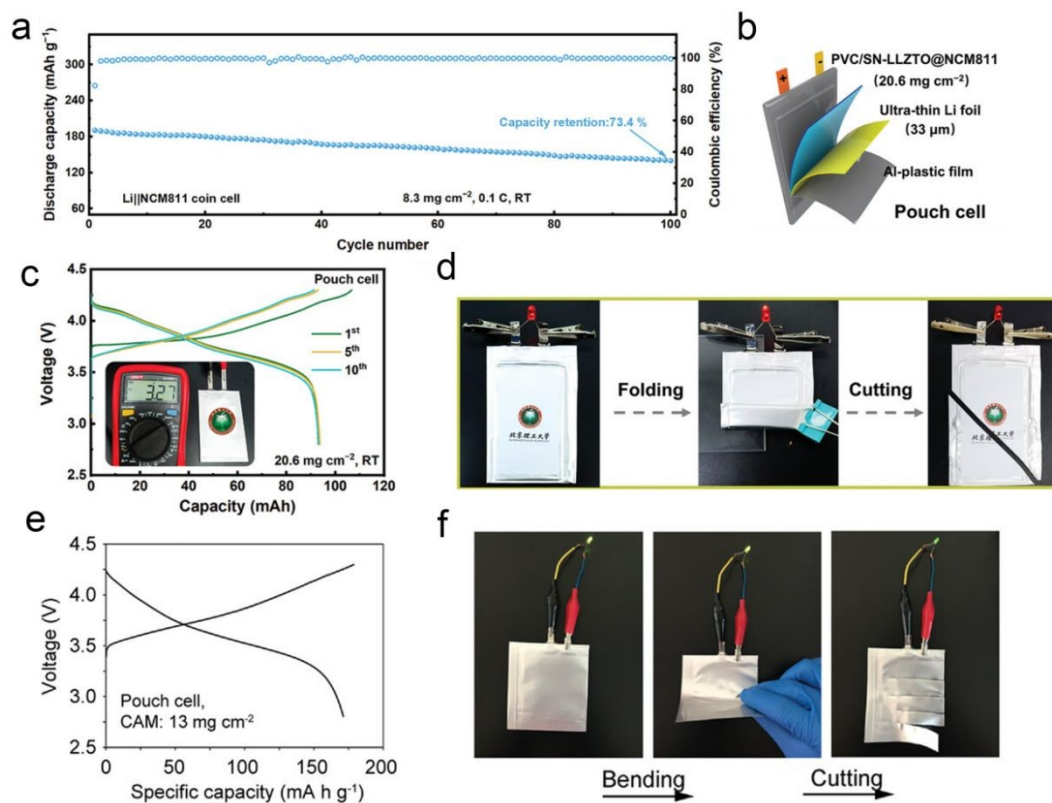
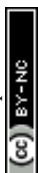


Fig. 23 a) Cycling stability and the corresponding coulombic efficiencies of Li||NCM811 full cells with cathode loading of 8.3 mg cm^{-2} at 0.1 C and RT. b) Schematic diagram of the pouch cell composed of the integrated PVC/SN-LLZTO@NCM811 and ultrathin Li foil. c) Charge and discharge voltage profiles of the Li||NCM811 pouch cell with NCM811 loading of 20.6 mg cm^{-2} at 0.05 C . d) The optical photograph of the pouch cell lightening a diode before and after folding and cutting tests. Reproduced with permission from ref. [150]. Copyright 2024, Wiley-VCH GmbH. The Li|UFF/PEO/PAN/LiTFSI|NCM811 pouch cell of e) the charge/discharge voltage profiles at the second cycle with a cathode active material (CAM) loading of 13 mg cm^{-2} at 0.45 mA cm^{-2} and f) powering a light-emitting diode under normal, bending, and cutting state. Reproduced with permission from ref. [160]. Copyright 2021, Wiley-VCH GmbH.

Although the ASSLIBs are regarded as one of the most promising options in the future electrochemical energy storage devices, its development is still limited by its low positive load and poor rate performance. Hu et al. develop a novel in situ polymerized integrated ultrathin PVC/SN-LLZTO SSE, which not only as a rigid scaffold to prevent direct contact between the cathode and anode but also as active inorganic fillers to enhance the mechanical properties of in situ polymerized SSE film[150]. In order to demonstrate the effects of the integrated ultrathin PVC/SN-LLZTO SSE in practical working conditions, they fabricated the Li||NCM811 full cells with an increased



NCM811 loading of 8.3 mg cm^{-2} . The cell with the PVC/SN-LLZTO SSE delivers a high initial discharge capacity of 190.7 mAh g^{-1} and achieves a 73.4% capacity retention after 100 cycles at 0.1 C (Fig. 23a). Considering the practical application potential of integrated ultrathin electrolyte/electrode structure design coupling with in situ polymerization, the pouch cells with ultrathin Li metal anodes ($33 \mu\text{m}$) and a high-loading NCM811 cathode (20.6 mg cm^{-2}) were prepared (Fig. 23b). The pouch cell can stably cycle and exhibits a high initial discharge capacity of 93 mAh (Fig. 23c). Moreover, the pouch cells with rationally designed LiF-rich SEI can cycle for >35 cycles. Furthermore, the pouch cells were subjected to a series of flexibility and safety tests. As shown in Fig. 23d, the solid-state pouch cell operates well to light up a red light-emitting diode bulb. Even under destructive conditions such as being folded and cut, the cells still exhibit reliability and high safety. For practical evaluation, the pouch cells are assembled based on the ultrathin fire-proof framework (UFF)/PEO/PAN/LiTFSI, thin Li foil, and high-loading NCM811 cathodes (13 mg cm^{-2}) with an area of 22 cm^2 , which exhibit a reversible capacity of 174 mAh g^{-1} (Fig. 23e). The pouch cell can easily power a light-emitting diode after charging to upper cut-off voltage. And bending the cell would not turn down the diode. Though the light shimmers after four-successive cuts to the pouch cell due to the loose electrode-electrolyte contact, the pouch cell shows a safe performance under severe conditions (Fig. 23f)[160].

5.3 Wide temperature range

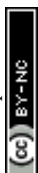
For wide temperature applications, polymer-based batteries are bound to face more complex performance requirements, including not only the performance of the electrolyte itself, but also the stability of the electrode-electrolyte interface. Low-temperature environments significantly reduce the ionic conductivity of polymers, as the Li^+ transport rate decreases exponentially with temperature, leading to larger energy barriers for electrochemical reactions and severe cell polarization. Low temperatures ultimately lead to a decrease in the ionic conductivity of the polymer and a decrease in the capacity of the polymer battery, even to the point of not being able to charge and



discharge properly. Polymers exhibit high ionic conductivity at high temperatures. However, the attendant difficulty is that the polymer tends to soften severely, shrink, and even decompose. Such events typically lead to battery failure or catastrophic events. Therefore, the application of polymers at elevated temperatures has focused on improving their high temperature stability and non-flammability. At elevated temperatures, the mechanical properties of polymer electrolytes deteriorate, reducing the ability to inhibit lithium dendrites and affecting performance and safety.

5.3.1 Adding fillers to reduce temperature sensitivity

The addition of fillers helps to improve the diffusion of lithium ions in polymers, thereby reducing their sensitivity to temperature changes. For example, Zhang et al. performed molecular dynamics simulations of PPC without LLZTO particles and PPC with LLZTO particles (PPCL) added electrolytes to study the diffusion behavior of Li^+ [161]. The addition of LLZTO increased the free volume of Li^+ moving in PPCL, which led to a rise in the diffusion coefficient from $4.5 \times 10^{-6} \text{ cm}^2 \text{ s}^{-1}$ to $6 \times 10^{-6} \text{ cm}^2 \text{ s}^{-1}$. Even at $0 \text{ }^\circ\text{C}$, this enhanced diffusion coefficient favors the charge/discharge performance of CPEs, and at such low temperatures, the discharge specific capacity of LiFePO_4 reaches 120 mAh g^{-1} at 0.1 C . The solid-state $\text{Li}||\text{LiFePO}_4$ cell was operated at $160 \text{ }^\circ\text{C}$, and can provide excellent multiplicity performance at high multiplicity, indicating that its prepared CPEs can be used in the field of high temperature lithium batteries. Cui et al. obtained a high modulus of $\approx 0.43 \text{ GPa}$ and a remarkable ionic conductivity of $6 \times 10^{-4} \text{ S cm}^{-1}$ at $30 \text{ }^\circ\text{C}$ using a 3D SiO_2 structure as the backbone [162]. In addition, the $\text{Li}||\text{LiFePO}_4$ cell performed well in the temperature range of 15 to $65 \text{ }^\circ\text{C}$, maintaining high capacity at low temperatures and approaching the theoretical capacity of LiFePO_4 at high temperatures (Fig. 24a). Hu et al. designed garnet frameworks with multi-scale aligned fine-scale structures using a wooden template (Fig. 24b), and prepared PEO-LLZO with good mechanical properties and ionic conductivity of 1.8×10^{-4} and $1.1 \times 10^{-3} \text{ S cm}^{-1}$ at RT and $90 \text{ }^\circ\text{C}$, respectively [163]. Therefore, optimizing the design and distribution of inorganic particle geometries is crucial for improving the ionic conductivity of CPEs.



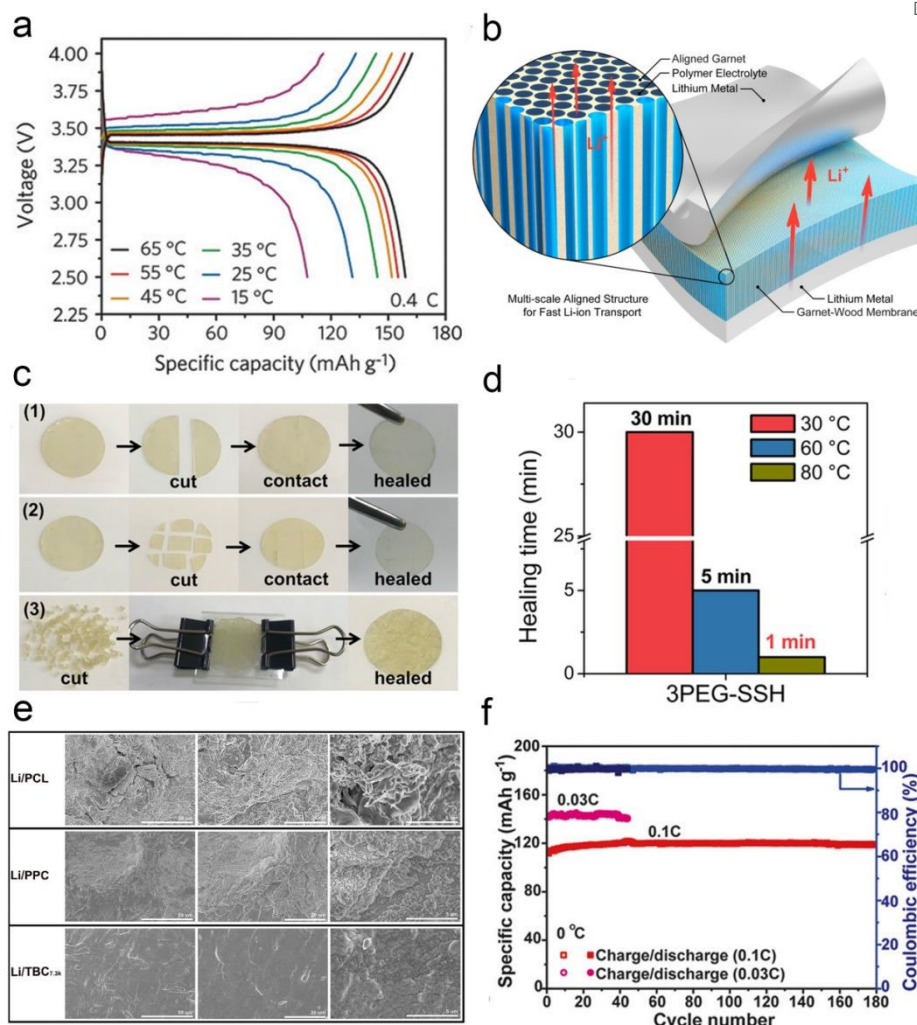


Fig. 24 a) Voltage profiles of the LiFePO₄-Li cells at various temperatures from 15 to 65 °C. Reproduced with permission from ref. [162]. Copyright 2018, Wiley-VCH GmbH. b) Schematic of multiscale aligned mesoporous garnet LLZO membrane incorporated with polymer electrolyte in a lithium symmetric cell. Reproduced with permission from ref. [163]. Copyright 2019, American Chemical Society. c) Photographs of disk-shaped 3PEG-SSH cut into different forms. d) Self-healing time of 3PEG-SSH. Reproduced with permission from ref. [164]. Copyright 2020, American Chemical Society. e) The SEM images of Li anodes using different electrolytes after 500 h Li/Li cycles. Reproduced with permission from ref. [165]. Copyright 2020, Elsevier. f) Galvanostatic cycling performances of Li|Homo-SPE|LiFePO₄ cells at 0 °C. Reproduced with permission from ref. [166]. Copyright 2020, Wiley-VCH GmbH.

5.3.2 Structural modifications to provide functional properties

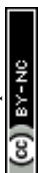
In contrast to the role of fillers in reinforcing the polymers, the modification of polymers also provides them with other functional properties such as self-healing, which are significantly enhanced at high temperatures, further improving the safety of polymers at high temperatures. Xue et al. synthesized a novel polymer containing



disulfide bonds and urea groups with self-healing function by cross-linking method [164]. As shown in Fig. 24c, the polymer was able to self-heal at RT without any other manipulation after different degrees of cracking. As the temperature increased from 30 °C to 80 °C, the repair time was rapidly reduced from 30 min to 1 min (Fig. 24d). The self-healing ability greatly ensures the safety of the battery at high temperatures. Structural modifications can improve its ability to inhibit the growth of lithium dendrites, thus reducing the risk of short-circuit at high temperatures. For example, Zhang et al. designed a BAB-type triblock copolymer (TBC) with PPC as the A-block and PCL as the B-block [165]. The triblock copolymer (PCL-PPC-PCL) exhibits high ionic conductivity ($3 \times 10^{-5} \text{ S cm}^{-1}$) and effectively inhibits lithium dendrite formation at 70 °C. As shown in Fig. 24e, the lithium metal surface in Li/PCL-PPC-PCL/Li remained relatively homogeneous after cycling at 70 °C for 500 h, whereas lithium symmetric batteries based on other monomers have shown a large amount of dead lithium. Chen et al. effectively inhibited the crystallization of PEO through the introduction of SN, while reducing the affinity between EO and Li^+ , resulting in a two-order-of-magnitude increase in the ionic conductivity of PEO [166]. LiFePO_4 based on this electrolyte can maintain 82% of the capacity of RT at 0 °C, showing excellent low-temperature performance (Fig. 24f).

5.4 Low external pressure

While solid-state electrolytes have received a lot of attention due to their high energy density and high safety, the external pressure during the operation of solid-state batteries has also received the attention of researchers. At present, the operation of solid-state batteries requires tens or even hundreds of megapascals of pressure to ensure the contact between the solid-state electrode and electrolyte interface, which greatly increases the cost of solid-state batteries and hinders the practical application of solid-state batteries. To solve the problem, Pan et al. [167] designed an elastic electrolyte based on a mixture of a dual monomer copolymer and a deep eutectic solvent, applying it to solid-state batteries to achieve stable operation without any external pressure, relying only on the internal pressure of the battery. In order to measure the internal



pressure, they developed a thin-film pressure-sensitive sensor (Fig. 25a), which measured the internal pressures of the button battery and the soft pack battery of 546 kPa and 52 kPa, respectively (Fig. 25b). These pressures are significantly lower than the conventional external pressure applied to solid-state batteries. The $\text{LiFePO}_4\|\text{Li}$ battery has a reversible specific capacity of 147.4 mAh g^{-1} , and can be stable for 400 cycles (Fig. 25c). $\text{LiFePO}_4\|\mu\text{m-Si}$ full battery can cycle for 150 cycles (Fig. 25d), and the soft-pack battery can still work under the shearing and bending conditions (Fig. 25e). Besides, under the guidance of "micro-viscosity control", Wang's team[168] made full use of the strong adsorption between polymer chains and ions to effectively regulate the condensed state structure of polymer electrolytes, successfully constructing a high-entropy polymer tape electrolyte (HETE) (Fig. 25f). By using the excellent surface adhesion characteristics of HETE, the in-situ interface bonding between electrolyte film and electrode was realized. After simple pressing and packaging, a flexible solid-state tape battery that can work without external pressure can be obtained. The electrochemical performance of the $\text{Li}|\text{HETE}|\text{LFP}$ tape battery was also evaluated and Fig. 25g shows the stable cycling performance at 0.1 C at 50 °C over 20 cycles. The solid-state tape battery has excellent interface stability and flexibility, maintaining interface stability without additional pressure, and can withstand extreme deformation such as distortion and compression.

View Article Online
DOI: 10.1039/D4MH01869A



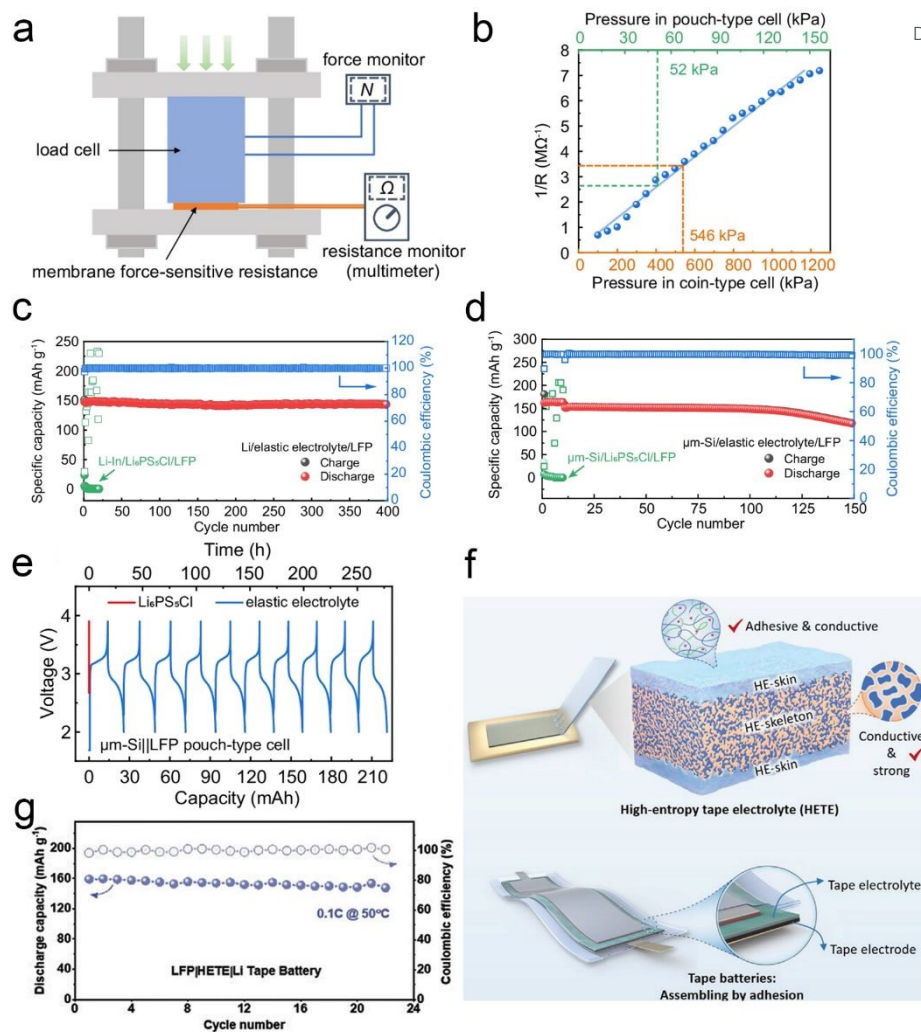
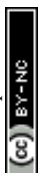


Fig. 25 a) Schematic of calibration of the membrane force-sensitive resistance (MFSR). b) The fitted standard response curve (blue) of resistance to pressure of the MFSR. The built-in pressure of the coin-type and pouch-type cell is indicated with orange and green dashed line, respectively. Electrochemical performance of SSBs using elastic electrolytes at zero applied pressure and relying only on the battery's built-in stress. c) Long cycle stability of LFP|| μ -Si full battery and d) LFP||Li battery. e) LFP|| μ -Si soft pack battery charge and discharge curve. Reproduced with permission from ref. [167]. Copyright 2024, Spring Nature. f) The schematic of high-entropy tape electrolyte (HETE) and compression-free solid-state tape batteries. g) Cycle performance of the LFP||Li tape batteries with HETE electrolytes at 50 °C. Reproduced with permission from ref. [168]. Copyright 2023, Wiley-VCH GmbH.



6 Summary and outlook

View Article Online
DOI: 10.1039/D4MH01869A

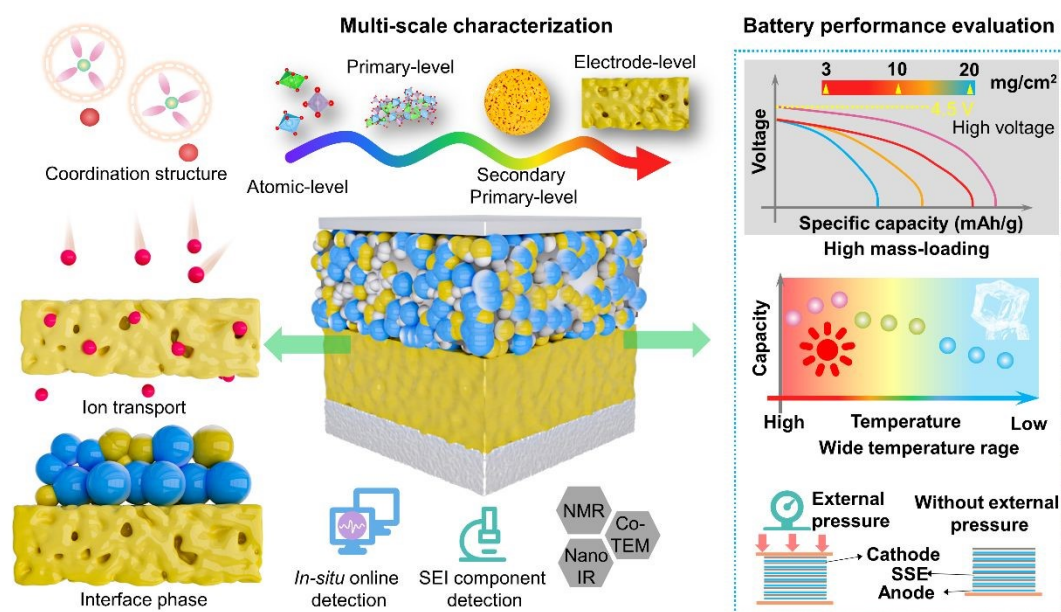


Fig. 26 The diagram of methods for achieving high performance of SSBs and factors for evaluating battery performance.

Solid-state electrolytes have gradually become a hot spot for the development of electric vehicle industry in recent years due to their high safety. Among these, polymer electrolytes have received wide attention for their simple preparation, flexibility, and better contact with electrodes. Therefore, this review introduces the ion transport mechanism of solid electrolytes, summarizes the advanced strategies for improving the ionic conductivity of polymer-inorganic solid electrolytes, and discusses the construction of electrode/electrolyte interface, systematically analyzing the electrochemical properties of polymer electrolytes. In general, polymer-inorganic solid electrolytes have become the current development hotspot of all-solid polymer-based lithium batteries, however, they still face many difficulties, such as low ionic conductivity, narrow electrochemical window, interface instability, and so on, which seriously limit their commercial development. In future research, realizing the high-performance application of polymer-based solid-state batteries is still a big challenge. Fig. 26 summarizes the approaches to achieving high performance in solid-state batteries from the following aspects and provides the elements of battery performance evaluation.

- (1) Li^+ coordination structure: The solvation structure is derived from the



competitive coordination of solvents and anions with Li^+ and is determined by many factors. The polarity of the components is one of the factors that affect their coordination with Li^+ . Selecting suitable ligands, controlling solvent environment, adjusting temperature and pressure, using auxiliary ligands and employing biomimetic design can improve the coordination structure, stability and function of lithium ions.

(2) Ion transport: Investigating the mechanisms by which the coordination structure affects ion transport and optimizing solvent-polymer-ion interactions in polymer electrolytes are essential. The design of SPEs that “decouples” the Li^+ movement and the segmented movement of the polymer not only can maintain the mechanical strength of the SPEs but also can promote ion transmission.

(3) Interface engineering: Regulating the interaction between electrolyte and electrode through interface engineering, optimizing the interface film-forming behavior, and improving the cycling stability and safety of batteries are crucial. Future development will focus on the design of polymer electrolytes with excellent interface stability to achieve the commercial application of high-performance lithium-ion batteries. The interface film-forming properties of electrolytes are improved by surface modification, interface modulation and interface design. These methods can help reduce the interface impedance between the electrolyte and the electrode, thereby improving the cycle life and safety of the battery.

(4) Multi-scale characterization: In solid electrolytes, ion migration is a multi-scale process, involving multiple scales from atoms to electrodes level. The detection of ion transport at different scales requires a combination of various characterization techniques to achieve effective observation. In-situ online characterization technique is very important for real-time monitoring of the reaction process in the working state of the battery, which is helpful for researchers to analyze the reaction mechanism. In addition, a series of advanced characterization methods, such as NMR, nano-IR, cryo-TEM, are also crucial for studying the surface interface and chemical processes of solid-state batteries.

In general, the current development of polymer-inorganic SSEs is a booming field



for sustainable energy-related materials and devices, and SSBs have a wide range of application prospects in new energy vehicles. Future research on SSEs can evaluate the electrochemical performance of SSBs by using parameters related to high voltage cathode, high mass-loading, wide temperature range, and low external pressure, thereby providing good safety, higher energy density, and longer cycle life.

View Article Online
DOI: 10.1039/D4MH01869A

Credit authorship contribution statement

Qingqing Zhou: Writing - original draft, Investigation, Formal analysis. **Minfeng Chen:** Software. **Junjie Lu:** Conceptualization. **Bifu Sheng:** Investigation. **Jizhang Chen:** Supervision. **Qiaobao Zhang:** Supervision. **Xiang Han:** Writing - review & editing, Supervision, Project administration, Funding acquisition.

Data availability

Data availability is not applicable to this article as no new data were created or analyzed in this study.

Conflicts of interest

The authors declare that they have no conflicts of interest.

Acknowledgement

This work was financially supported by the National Natural Science Foundation of China (22209075, 92472104, 52122211).

References

- [1] M. Wakihara, *Mat. Sci. Eng. R*, 2001, **33**, 109–134.
- [2] S.B. Ge, K.X. Wei, W.X. Peng, R.Z. Huang, E. Akinlabi, H.Y. Xia, M.W. Shahzad, X.H. Zhang, B.B. Xu, J.C. Jiang, *Chem. Soc. Rev.*, 2024, **23**, 11259–11302.
- [3] K. Xu, *Chem. Rev.*, 2004, **104**, 4303–4418.
- [4] J.X. Liu, S. Ihuaenyi, R. Kuphal, J. Salinas, L. Xie, L. Yang, U. Janakiraman, M.E. Fortier, C.C. Fang, *J. Electrochem. Soc.*, 2023, **170**, 010535.
- [5] D.X. Ouyang, K. Wang, Y.M. Pang, Z.R. Wang, *ACS Appl. Energy Mater.*, 2023, **6**, 2063–2071.
- [6] C.C. Su, M.N. He, J.Y. Shi, R. Amine, Z. Yu, L. Cheng, J.C. Guo, K. Amine,



- Energy Environ. Sci., 2021, **14**, 3029–3034.
- [7] J. Liu, Z.N. Bao, Cui, Y., E.J. Dufek, J.B. Goodenough, P. Khalifah, Q.Y. Li, B.Y. Liaw, P. Liu, A. Manthiram, Y.S. Meng, V.R. Subramanian, M.F. Toney, V.V. Viswanathan, M.S. Whittingham, J. Xiao, W. Xu, J.H. Yang, X.Q. Yang, J.G. Zhang, *Nat. Energy*, 2019, **4**, 180–186.
- [8] J.B. Goodenough, H.P. Hong, J. Kafalas, *Mater. Res. Bull.*, 1976, **11**, 203–220.
- [9] H.Y.P. Hong, *Mater. Res. Bull.*, 1978, **13**, 117–124.
- [10] J. Fu, *Solid State Ion.*, 1997, **104**, 191–194.
- [11] J. Fu, *Solid State Ion.*, 1997, **96**, 195–200.
- [12] Y. Inaguma, C. Liqun, M. Itoh, T. Nakamura, T. Uchida, H. Ikuta, M. Wakihara, *Solid State Commun.*, 1993, **86**, 689–693.
- [13] R. Murugan, V. Thangadurai, W. Weppner, *Angew. Chem. Int. Ed.*, 2007, **46**, 7778–7781.
- [14] R. Koerver, I. Aygün, T. Leichtweiß, C. Dietrich, W. Zhang, J.O. Binder, P. Hartmann, W.G. Zeier, J. Janek, *Chem. Mater.*, 2017, **29**, 5574–5582.
- [15] X.G. Han, Y.H. Gong, K. Fu, X.F. He, G.T. Hitz, J.Q. Dai, A. Pearse, B.Y. Liu, H. Wang, G. Rubloff, Y.F. Mo, V. Thangadurai, E.D. Wachsman, L.B. Hu, *Nat. Mater.*, 2017, **16**, 572–579.
- [16] H.J. Deiseroth, S.T. Kong, H. Eckert, J. Vannahme, C. Reiner, T. Zaiß, M. Schlosser, *Angew. Chem. Int. Ed.*, 2008, **47**, 755–758.
- [17] N. Kamaya, K. Homma, Y. Yamakawa, M. Hirayama, R. Kanno, M. Yonemura, T. Kamiyama, Y. Kato, S. Hama, K. Kawamoto, A. Mitsui, *Nat. Mater.*, 2011, **10**, 682–686.
- [18] Y. Seino, T. Ota, K. Takada, A. Hayashi, M. Tatsumisago, *Energy Environ. Sci.*, 2014, **7**, 627–631.
- [19] Y. Kato, S. Hori, T. Saito, K. Suzuki, M. Hirayama, A. Mitsui, M. Yonemura, H. Iba, R. Kanno, *Nat. Energy*, 2016, **1**, 16030.
- [20] M.A. Kraft, S.P. Culver, M. Calderon, F. Bocher, T. Krauskopf, A. Senyshyn, C. Dietrich, A. Zevalkink, J. Janek, W.G. Zeier, *J. Am. Chem. Soc.*, 2017, **139**, 10909–10918.
- [21] J. Lee, T. Lee, K. Char, K.J. Kim, J.W. Choi, *Acc. Chem. Res.*, 2021, **54**, 3390.
- [22] H. Wang, H. An, H. Shan, L. Zhao, J. Wang, *Acta Phys. Chim. Sin.*, 2021, **37**, 2007070.
- [23] L.L. Liu, F. Wu, H. Li, L.Q. Chen, *J. Chin. Ceram. Soc.*, 2019, **47**, 1367–1385.
- [24] Y.K. Liu, T. Yu, S.H. Guo, H.S. Zhou, *Acta Phys. Chim. Sin.*, 2023, **39**, 2301027.
- [25] B. He, F. Zhang, Y. Xin, C. Xu, X. Hu, X. Wu, Y. Yang, H. Tian, *Nat. Rev. Chem.*, 2023, **7**, 826–842.
- [26] W. Weppner, R.A. Huggins, *Physics Letters A*, 1976, **58**, 245–248.
- [27] R. Kanno, Y. Takeda, O. Yamamoto, *Mater. Res. Bull.*, 1981, **16**, 999–1005.
- [28] Y. Tomita, H. Matsushita, K. Kobayashi, Y. Maeda, K. Yamada, *Solid State Ion.*, 2008, **179**, 867–870.
- [29] T. Asano, A. Sakai, S. Ouchi, M. Sakaida, A. Miyazaki, S. Hasegawa, *Adv. Mater.*, 2018, **30**, 1803075.
- [30] X. Li, J. Liang, N. Chen, J. Luo, K.R. Adair, C.H. Wang, M.N. Banis, T.K. Sham,



- L. Zhang, S.Q. Zhao, S.G. Lu, H. Huang, R.Y. Li, X.L. Sun, *Angew. Chem.* **2019**, **131**, 16579–16584. View Article Online
DOI: 10.1039/D4MH01869A
- [31] Q. Zhang, K. Liu, K. Liu, L. Zhou, C. Ma, Y. Du, *Electrochim. Acta*, **2020**, **351**, 136342.
- [32] D.E. Fenton, *Polymer*, **1973**, **14**, 589.
- [33] C. Berthier, W. Gorecki, M. Minier, M.B. Armand, J.M. Chabagno, P. Rigaud, *Solid State Ion.*, **1983**, **11**, 91–95.
- [34] K. Tsunemi, H. Ohno, E. Tsuchida, *Electro. Acta*, **1983**, **28**, 833–837.
- [35] M. Watanabe, M. Kanba, K. Nagaoka, I. Shinohara, *J. Polym. Sci. Pol. Phys.*, **1983**, **21**, 939–948.
- [36] M. Alamgir, R.D. Moulton, K.M. Abraham, *Electro. Acta*, **1991**, **36**, 773–782.
- [37] X.Y. Wei, D.F. Shriver, *Chem. Mater.*, **1998**, **10**, 2307–2308.
- [38] J. Wu, S. Liu, F. Han, X. Yao, C. Wang, *Adv. Mater.*, **2021**, **33**, 2000751.
- [39] T. Famprakis, P. Canepa, J.A. Dawson, M.S. Islam, C. Masquelier, *Nat. Mater.*, **2019**, **18**, 1278–1291.
- [40] Q. Zhao, S. Stalin, C.Z. Zhao, L. A. Archer, *Nat. Rev. Mater.*, **2020**, **5**, 229–252.
- [41] A. Manthiram, X.W. Yu, S.F. Wang, *Nat. Rev. Mater.*, **2017**, **2**, 16103.
- [42] Z. Liu, W. Fu, E.A. Payzant, X. Yu, Z. Wu, N.J. Dudney, J. Kiggans, K. Hong, A.J. Rondinone, *J. Am. Chem. Soc.*, **2013**, **135**, 975–978.
- [43] H. Tsukasaki, S. Mori, H. Morimoto, A. Hayashi, M. Tatsumisago, *Scientific Reports*, **2017**, **7**, 4142.
- [44] S. Breuer, M. Uitz, H.M.R. Wilkening, *J. Phys. Chem. Lett.*, **2018**, **9**, 2093–2097.
- [45] J.F. Wu, X. Guo, *Phys. Chem. Chem. Phys.*, **2017**, **19**, 5880–5887.
- [46] J.A. Dawson, P. Canepa, T. Famprakis, C. Masquelier, M.S. Islam, *J. Am. Chem. Soc.*, **2018**, **140**, 362–368.
- [47] A. Sakuda, A. Hayashi, M. Tatsumisago, *Chem. Mater.*, **2010**, **22**, 949–956.
- [48] C. Yu, S. Ganapathy, E.R.H. Eck, H. Wang, S. Basak, Z. Li, M. Wagemaker, *Nat. Commun.*, **2017**, **8**, 1086.
- [49] D. Lu, R. Li, M.M. Rahman, P. Yu, L. Lv, S. Yang, Y. Huang, C. Sun, S. Zhang, H. Zhang, J. Zhang, *Nature*, **2024**, **627**, 101–107.
- [50] L. Yue, J. Ma, J. Zhang, J. Zhao, S. Dong, Z. Liu, G. Cui, L. Chen, *Energy Storage Mater.*, **2016**, **5**, 139–164.
- [51] A.S. Shaplov, R. Marcilla, D. Mecerreyes, *Electrochim. Acta*, **2015**, **175**, 18–34.
- [52] K.S. Ngai, S. Ramesh, K. Ramesh, J.C. Juan, *Ionics*, **2016**, **22**, 1259–1279.
- [53] X. Lu, Y. Wang, X. Xu, B. Yan, T. Wu, L. Lu, *Adv. Energy Mater.*, **2023**, **13**, 2301746.
- [54] L.Z. Fan, H.C. He, C.W. Nan, *Nat. Rev. Mater.*, **2021**, **6**, 1003–1019.
- [55] P. Yadav, M.S. Hosen, P.K. Dammala, P. Ivanchenko, J.V. Mierlo, M. Bercibar, *Solid State Ion.*, **2023**, **399**, 116308.
- [56] F. Wu, Z. Wen, Z. Zhao, J. Bi, Y. Shang, Y. Liang, L. Li, N. Chen, Y. Li, R. Chen, *Energy Storage Mater.*, **2021**, **38**, 447–453.
- [57] D. Lin, W. Liu, Y. Liu, H.R. Lee, P.C. Hsu, K. Liu, Y. Cui, *Nano Lett.*, **2016**, **16**, 459–465.
- [58] G.X. Wang, L. Yang, J.Z. Wang, H.K. Liu, S.X. Dou, *J. Nanosci. Nanotech.*,



- 2005, **5**, 1135–1140.
- [59] C. Hu, Y. Shen, M. Shen, X. Liu, H. Chen, C. Liu, T. Kang, F. Jin, L. Li, J. Li, Y. Li, N. Zhao, X. Guo, *J Am. Chem. Soc.*, 2020, **142**, 18035–18041.
- [60] H. Gao, N.S. Grundish, Y. Zhao, A. Zhou, J.B. Goodenough, *Energy Mater. Adv.*, 2021, 1932952.
- [61] Y.W. Chen-Yang, H.C. Chen, F.J. Lin, C.C. Chen, *Solid State Ion.*, 2002, **150**, 327–335.
- [62] W. Liu, S.W. Lee, D. Lin, F. Shi, S. Wang, A.D. Sendek, Y. Cui, *Nature energy*, 2017, **2**, 1–7.
- [63] Z. Li, H.M. Huang, J.K. Zhu, J.F. Wu, H. Yang, L. Wei, X. Guo, *ACS Appl. Mater. Interfaces*, 2018, **11**, 784–791.
- [64] S.S. Chi, Y. Liu, N. Zhao, X. Guo, C.W. Nan, L.Z. Fan, *Energy Storage Mater.*, 2019, **17**, 309–316.
- [65] C. Wang, Y. Yang, X. Liu, H. Zhong, H. Xu, Z. Xu, H. Shao, F. Ding, *ACS Appl. Mater. Interfaces*, 2017, **9**, 13694–13702.
- [66] J. Li, K. Zhu, Z. Yao, G. Qian, J. Zhang, K. Yan, J. Wang, *Ionics*, 2020, **26**, 1101–1108.
- [67] P. Shi, J. Ma, M. Liu, S. Guo, Y. Huang, S. Wang, L. Zhang, L. Chen, K. Yang, X. Liu, Y. Li, X. An, *Nat. Nanotech.*, 2023, 1–9.
- [68] Q. Wu, M. Fang, S. Jiao, S. Li, S. Zhang, Z. Shen, *Nat. Commun.*, 2023, **14**, 6296.
- [69] H. Yang, B. Zhang, M.X. Jing, X.Q. Shen, L. Wang, H. Xu, X.H. Yan, X.M. He, *Adv. Energy Mater.*, 2022, **12**, 2201762.
- [70] K.X. Mu, D. Wang, W.L. Dong, Q. Liu, Z.N. Song, W.J. Xu, P.P. Yao, Y.A. Chen, B. Yang, C.H. Li, L. Tian, C.Z. Zhu, J. Xu, *Adv. Mater.*, 2023, **35**, 2304686.
- [71] Z.H. Ren, J.X. Li, M.H. Cai, R.N. Yin, J.N. Liang, Q.L. Zhang, C.X. He, X.T. Jiang, X.Z. Ren, *J. Mater. Chem. A*, 2023, **11**, 1966–1977.
- [72] S.Q. Huang, Z.L. Cui, L.X. Qiao, G.J. Xu, J.J. Zhang, K. Tang, X.C. Liu, Q.L. Wang, X.H. Zhou, B.T. Zhang, G.L. Cui, *Electrochim. Acta*, 2019, **299**, 820–827.
- [73] K. Yang, L.K. Chen, J.B. Ma, C. Lai, Y.F. Huang, J.S. Mi, J. Biao, D.F. Zhang, P.R. Shi, H.Y. Xia, G.M. Zhong, F.Y. Kang, Y.B. He, *Angew. Chem. Int. Ed.*, 2021, **60**, 24668–24675.
- [74] W.W. Li, C.Z. Sun, J. Jin, Y.P. Li, C.H. Chen, Z.Y. Wen, *J. Mater. Chem. A*, 2019, **7**, 27304–27312.
- [75] H.T. Zhang, Y.C. Wang, J.F. Huang, W. Li, X.K. Zeng, A.L. Jia, H.Z. Peng, X. Zhang, W.Q. Yang, *Energy Environ. Mater.*, 2024, **7**, e12514.
- [76] B. Tong, Z. Song, H. Wu, X. Wang, W. Feng, Z. Zhou, H. Zhang, *Mater. Futures*, 2022, **1**, 042103.
- [77] M. Armand, J.M. Chabagno, M.J. Duclot, *Fast Ion Transp. Solids: Electrodes Electrolytes*, *Proc. Int. Conf.*, 1979, 131–136.
- [78] Z. Stoeva, I. Martin-Litas, E. Staunton, Y.G. Andreev, P.G. Bruce, *J. Am. Chem. Soc.*, 2003, **125**, 4619–4626.
- [79] C. Zhang, Y.G. Andreev, P.G. Bruce, *Angew. Chem. Int. Ed.*, 2007, **46**, 2848–2850.



- [80] C. Zhang, S. Gamble, D. Ainsworth, A.M.Z. Slawin, Y.G. Andreev, P.G. Bruce, *Nat. Mater.*, 2009, **8**, 580–584. View Article Online
DOI: 10.1039/D4MH01869A
- [81] C.A. Angell, J. Fan, C. Liu, Q. Lu, E. Sanchez, K. Xu, *Solid State Ion.*, 1994, **69**, 343–353.
- [82] C.A. Angell, C. Liu, E. Sanchez, *Nature*, 1993, **362**, 137–139.
- [83] Y. Takahashi, H. Tadokoro, *Macromol.*, 1973, **6**, 672–675.
- [84] P. Johansson, *Polymer*, 2001, **42**, 4367–4373.
- [85] C.D. Robitaille, D.J. Fauteux, *Electrochem. Soc.*, 1986, **133**, 315.
- [86] D.G.H. Ballard, P. Cheshire, T.S. Mann, J.E. Przeworski, *Macromol.*, 1990, **23**, 1256–1264.
- [87] G. Orädd, L. Edman, A. Ferry, *Solid State Ion.*, 2002, **152**, 131–136.
- [88] G. Zardalidis, E. Ioannou, S. Pispas, G. Floudas, *Macromol.*, 2013, **46**, 2705–2714.
- [89] H. Jiang, Q. Zhang, Y. Zhang, L. Sui, G. Wu, K. Yuan, X. Yang, *Phys. Chem. Chem. Phys.*, 2019, **21**, 10417–10422.
- [90] S. Han, *Sci. Rep.*, 2019, **9**, 1–10.
- [91] J. Zheng, Y.Y. Hu, *ACS Appl. Mater. Interfaces*, 2018, **10**, 4113–4120.
- [92] H. Lee, M. Yanilmaz, O. Toprakci, K. Fu, X. Zhang, *Energy Environ. Sci.*, 2014, **7**, 3857–3886.
- [93] S.A. Pervez, G. Kim, B.P. Vinayan, M.A. Cambaz, M. Kuenzel, M. Hekmatfar, M. Fichtner, *Small*, 2020, **16**, 2000279.
- [94] Q. Zhang, K. Liu, K. Liu, J. Li, C. Ma, L. Zhou, Y. Du, *J. Colloid Interface Sci.*, 2020, **580**, 389–398.
- [95] J. Zagórski, J.M. López del Amo, M.J. Cordill, F. Aguesse, L. Buannic, *ACS Applied Energy Mater.*, 2019, **2**, 1734–1746.
- [96] J.G. Connell, T. Fuchs, H. Hartmann, T. Krauskopf, Y.S. Zhu, J. Sann, R. Garcia-Mendez, J. Sakamoto, S. Tepavcevic, J. Janek, *Chemistry of Mater.*, 2020, **32**, 10207–10215.
- [97] T. Jiang, P. He, G. Wang, Y. Shen, C.W. Nan, L.Z. Fan, *Adv. Energy Mater.*, 2020, **10**, 1903376.
- [98] H. Yamada, D. Tsunoe, S. Shiraishi, G. Isomichi, *J. Phys. Chem. C*, 2015, **119**, 5412–5419.
- [99] M. Agostini, Y. Aihara, T. Yamada, *J. Electro. Soc.* 2013, **244**, 48–51.
- [100] Q. Zhang, Y.Q. Kong, K.X. Gao, Y.J. Wen, Q. Zhang, H.Y. Fang, C.J. Ma, Y.P. Du, *Sci. China Technol. Sci.*, 2022, **65**, 2246–2258.
- [101] B. Jiang, J. Iocozzia, L. Zhao, H.F. Zhang, Y.W. Harn, Y.H. Chen, Z.Q. Lin, *Chem. Soc. Rev.*, 2019, **48**, 1194–1228.
- [102] Y.P. Guo, R.Y. Wang, C. Cui, R.D. Xiong, Y.Q. Wei, T.Y. Zhai, H.Q. Li, *Nano Lett.*, 2020, **20**, 7680–7687.
- [103] K. Takada, N. Ohta, L.Q. Zhang, X.X. Xu, B.T. Hang, T. Ohnishi, M. Osada, T. Sasaki, *Solid State Ion.*, 2012, **225**, 594–597.
- [104] B.B. Wu, S.Y. Wang, W.J. Evans IV, D.Z. Deng, J.H. Yang, J. Xiao, *J. Mater. Chem. A*, 2016, **4**, 15266–15280.
- [105] C. Yada, C.E. Lee, D. Laughman, L. Hannah, H. Iba, B.E. Hayden, J.



- Electrochem. Soc., 2015, **162**, A722–A726.
- [106] S.H. Xia, Y. Zhao, J.H. Yan, J.Y. Yu, B. Ding, *ACS Nano*, 2021, **15**, 3161–3170.
- [107] H. Yamada, A.J. Bhattacharyya, J. Maier, *Adv. Funct. Mater.*, 2006, **16**, 525–530.
- [108] D. Zhang, Y. Liu, S. Yang, J. Zhu, H. Hong, S. Li, Q. Xiong, Z. Huang, S. Wang, J. Liu, C. Zhi, *Adv. Mater.*, 2024, 2401549.
- [109] W. Zhang, V. Koverga, S. Liu, J. Zhou, J. Wang, P. Bai, S. Tan, N.K. Dandu, Z. Wang, F. Chen, J. Xia, H.L. Wan, X.Y. Zhang, H.C. Yang, B.L. Lucht, A.M. Li, X.Q. Yang, E.Y. Hu, S.R. Raghavan, A.T. Ngo, C.S. Wang, *Nature Energy*, 2024, **9**, 386–400.
- [110] L. Pan, S. Sun, G. Yu, X.X. Liu, S. Feng, W. Zhang, M. Turgunov, Y. Wang, Z.M. Sun, *Chem. Eng. J.*, 2022, **449**, 137682.
- [111] S.M. Wu, Lanzhou University of Technology, 2020.
- [112] P. Yao, B. Zhu, H. Zhai, X. Liao, Y. Zhu, W. Xu, Q. Cheng, C. Jayyosi, Z. Li, J. Zhu, K.M. Myers, X. Chen, Y. Yang, *Nano Lett.*, 2018, **18**, 6113–6120.
- [113] M.M. Heravi, M. Ghavidel, L. Mohammadkhani, *RSC Adv.*, 2018, **8**, 27832.
- [114] J. Lang, Y. Long, J. Qu, X. Luo, H. Wei, K. Huang, H. Zhang, L. Qi, Q. Zhang, Z. Li, H. Wu, *Energy Storage Mater.*, 2019, **16**, 85–90.
- [115] X. Zhang, J. Han, X. Niu, C. Xin, C. Xue, S. Wang, Y. Shen, L. Zhang, L. Li, C.W. Nan, *Batteries Supercaps*, 2020, **3**, 876–883.
- [116] Y. Liu, X. An, K. Yang, J. Ma, J. Mi, D. Zhang, X. Cheng, Y. Li, Y. Ma, M. Liu, F. Kang, Y.B. He, *Energy Environ. Sci.*, 2024, **17**, 344–353.
- [117] P.B. Zhai, Z.L. Yang, Y. Wei, X.X. Guo, Y.J. Gong, *Adv. Energy Mater.*, 2022, **12**, 2200967.
- [118] T. Liu, Y. Zhang, R. Chen, S.X. Zhao, Y. Lin, C.W. Nan, Y. Shen, *Electrochem. Commun.*, 2017, **79**, 1–4.
- [119] B. He, F. Zhang, Y. Xin, C. Xu, X. Hu, X. Wu, Y. Yang, H. Tian, *Nat. Rev. Chem.*, 2023, **7**, 826–842.
- [120] Y. Huang, B. Chen, J. Duan, F. Yang, T. Wang, Z. Wang, W. Yang, C. Hu, W. Luo, Y. Huang, *Angew. Chem.*, 2020, **132**, 3728–3733.
- [121] K. Nie, Y. Hong, J. Qiu, Q. Li, X. Yu, H. Li, L. Chen, *Front. Chem.*, 2018, **6**, 616.
- [122] D. Lu, Y.F. Chen, W.W. Sun, W. Xie, S.Y. Yi, S.Q. Luo, L.L. Zuo, Y.S. Zhao, T.Y. Yang, P.T. Xiao, C.M. Zheng, *Adv. Energy Mater.*, 2023, **13**, 2301765.
- [123] S.K. Heiskanen, J. Kim, B.L. Lucht, *Joule*, 2019, **3**, 2322–2333.
- [124] Z. Zhang, K. Smith, R. Jervis, P.R. Shearing, T.S. Miller, D.J.L. Brett, *ACS Appl. Mater. Interfaces*, 2020, **12**, 35132–35141.
- [125] J. Xu, Y. Dou, Z. Wei, J. Ma, Y. Deng, Y. Li, H. Liu, S. Dou, *Adv. Sci.*, 2017, **4**, 1700146.
- [126] L. Xing, X. Zheng, M. Schroeder, J. Alvarado, A. W. Cresce, K. Xu, Q. Li, W. Li, *Acc. Chem. Res.*, 2018, **51**, 282–289.
- [127] Y.X. Yao, N. Yao, X.R. Zhou, Z.H. Li, X.Y. Yue, C. Yan, Q. Zhang, *Adv. Mater.*, 2022, **34**, 2206448.
- [128] X. Fan, C. Wang, *Chem. Soc. Rev.*, 2021, **50**, 10486–10566.
- [129] Z. Zhang, T. Yao, E. Wang, B. Sun, K. Sun, Z. Peng, *ACS Appl. Mater. Interfaces*,



- 2022, **14**, 45484–45493.
- [130] K. An, A.H.T. Tran, S. Kwak, J. Han, S.W. Song, *Adv. Funct. Mater.*, 2021, **31**, 2106102.
- [131] H. Kim, K. Lim, G. Yoon, J.H. Park, K. Ku, H.D. Lim, Y.E. Sung, K. Kang, *Adv. Energy Mater.*, 2017, **7**, 1700418.
- [132] J.Y. Liang, Y. Zhang, S. Xin, S.J. Tan, X.H. Meng, W.P. Wang, J.L. Shi, Z.B. Wang, F. Wang, L.J. Wan, G.Y. Guo, *Angew. Chem. Inter. Edi.*, 2023, **62**, e202300384.
- [133] J.M. Tarascon, M. Armand, *Nature*, 2001, **414**, 359–367.
- [134] R. Wang, W. Cui, F. Chu, F. Wu, *J. Energy Chem.*, 2020, **48**, 145–159.
- [135] M. Li, H. An, Y. Song, Q. Liu, J. Wang, H. Huo, S. Lou, J. Wang, *J. Am. Chem. Soc.*, 2023, **145**, 25632–25642.
- [136] Z. Li, R. Yu, S. Weng, Q. Zhang, X. Wang, X. Guo, *Nat. Commun.*, 2023, **14**, 482.
- [137] M. Zhao, J. Zhang, C.M. Costa, S. Lanceros-Méndez, Q. Zhang, W. Wang, *Adv. Mater.*, 2024, **36**, 2308590.
- [138] M.N. Obrovac, L. Christensen, D.B. Le, J.R. Dahn, *J. Electrochem. Soc.*, 2007, **154**, 849.
- [139] C. Wang, C. Yang, Z. Zheng, *Adv. Sci.*, 2022, **9**, 2105213.
- [140] R. Endo, T. Ohnishi, K. Takada, T. Masuda, *J. Phys. Chem. Lett.*, 2020, **11**, 6649–6654.
- [141] L.H. Gu, J.J. Han, M.F. Chen, W.J. Zhou, X.F. Wang, M. Xu, H.C. Lin, H.D. Liu, H.X. Chen, J.Z. Chen, Q.B. Zhang, X. Han, *Energy Storage Mater.*, 2022, **52**, 547–561.
- [142] X. Han, L.H. Gu, Z.F. Sun, M.F. Chen, Y.G. Zhang, L.S. Luo, M. Xu, S.Y. Chen, H.D. Liu, J.Y. Wan, Y.B. He, J. Chen, *Energy Environ. Sci.*, 2023, **16**, 5395–5408.
- [143] Y.G. Lee, S. Fujiki, C. Jung, N. Suzuki, N. Yashiro, R. Omoda, D.S. Ko, T. Shiratsuchi, T. Sugimoto, S. Ryu, J.H. Ku, T. Watanabe, Y. Park, Y. Aihara, D. Im, I.T. Han, *Nature Energy*, 2020, **5**, 299–308.
- [144] Z. Zhang, Z. Sun, X. Han, Y. Liu, S. Pei, Y. Li, L. Luo, P. Su, C. Lan, Z. Zhang, S. Xu, S. Guo, *Energy Environ. Sci.*, 2024, **17**, 1061–1072.
- [145] B.H. Wang, T. Xia, Q. Chen, Y.F. Yao, *Polymers*, 2020, **12**, 391.
- [146] X. Lei, J. Zhao, J. Wang, D. Su, *Sci. Chin. Chem.*, 2024, **67**, 291–311.
- [147] R. Lin, Y. He, C. Wang, P. Zou, E. Hu, X.Q. Yang, K. Xu, H.L. Xin, *Nat. Nanotech.*, 2022, **17**, 768–776.
- [148] M. Heber, K. Hofmann, C. Hess, *Batteries*, 2022, **8**, 10.
- [149] K. Chrissopoulou, K.S. Andrikopoulos, S. Fotiadou, S. Bollas, C. Karageorgaki, D. Christofilos, G.A. Voyiatzis, S.H. Anastasiadis, *Macromol.*, 2011, **44**, 9710–9722.
- [150] J.K. Hu, Y.C. Gao, S.J. Yang, X.L. Wang, X. Chen, Y.L. Liao, S. Li, J. Liu, H. Yuan, J.Q. Huang, *Adv. Funct. Mater.*, 2024, 2311633.
- [151] J.N. Liang, Y.P. Sun, Y. Zhao, Q. Sun, J. Luo, F.P. Zhao, X.T. Lin, X. Li, R.Y. Li, L. Zhang, S.G. Lu, H. Huang, X.L. Sun, *J. Mater. Chem. A*, 2020, **8**, 2769–2776.



- [152] J. Shen, Z. Lei, C. Wang, *Chem. Engin. J.*, 2022, **447**, 137503.
- [153] K. He, C. Chen, R. Fan, C. Liu, C. Liao, Y. Xu, J. Tang, R.K.Y. Li, *Compos. Sci. Technol.*, 2019, **175**, 28–34.
- [154] C.Z. Zhao, X.Q. Zhang, X.B. Cheng, R. Zhang, R. Xu, P.Y. Chen, H.J. Peng, J.Q. Huang, Q. Zhang, *Proc. Natl. Acad. Sci.*, 2017, **114**, 11069–11074.
- [155] L. Chen, Y. Li, S.P. Li, L.Z. Fan, C.W. Nan, J.B. Goodenough, *Nano Energy*, 2018, **46**, 176–184.
- [156] X.F. Yang, M. Jiang, X.J. Gao, D.N. Bao, Q. Sun, N. Holmes, H. Duan, S. Mukherjee, K. Adair, C.T. Zhao, J.W. Liang, W.H. Li, J.J. Li, Y. Liu, H. Huang, L. Zhang, S.G. Lu, Q.W. Lu, R.Y. Li, C.V. Singh, X.L. Sun, *Energy Environ. Sci.*, 2020, **13**, 1318–1325.
- [157] J. Liu, K. Liang, H. Duan, G. Chen, Y. Deng, *ACS Appl. Mater. Interfaces*, 2023, **15**, 57293–57303.
- [158] W. Han, J. Zheng, H. Huang, H. Zhou, H. Li, H. Zhang, L. Li, W. Zhou, B. An, C. Sun, *J. Membrane Sci.*, 2024, 123374.
- [159] R. Liao, C. Li, M. Zhou, R. Liu, S. Liu, D. Wu, *Chem. Sci.*, 2024.
- [160] F. He, W. Tang, X. Zhang, L. Deng, J. Luo, *Adv. Mater.*, 2021, **33**, 2105329.
- [161] J.J. Zhang, X. Zang, H.J. Wen, T.T. Dong, J.C. Chai, Y. Li, B.B. Chen, J.W. Zhao, S.M. Dong, J. Ma, L.P. Yue, Z.H. Liu, X.X. Guo, G.L. Cui, L.Q. Chen, *J. Mater. Chem. A*, 2017, **5**, 4940–4948.
- [162] D. Lin, P.Y. Yuen, Y. Liu, W. Liu, N. Liu, R.H. Dauskardt, Y. Cui, *Adv. Mater.*, 2018, **30**, 1802661.
- [163] J.Q. Dai, K. Fu, Y.H. Gong, J.W. Song, C.J. Chen, Y.G. Yao, G. Pastel, L. Zhang, E. Wachsman, L.B. Hu, *ACS Mater. Lett.*, 2019, **1**, 354–361.
- [164] Y.H. Jo, S. Li, C. Zuo, Y. Zhang, H. Gan, S. Li, L. Yu, D. He, X. Xie, Z. Xue, *Macromol.*, 2020, **53**, 1024–1032.
- [165] B. Zhang, Y. Liu, X. Pan, J. Liu, K. Doyle-Davis, L. Sun, J. Liu, X. Jiao, J. Jie, H. Xie, X. Sun, *Nano Energy*, 2020, **72**, 104690.
- [166] S. Xu, Z. Sun, C. Sun, F. Li, K. Chen, Z. Zhang, G. Hou, H.M. Cheng, F. Li, *Adv. Funct. Mater.*, 2020, **30**, 2007172.
- [167] H. Pan, L. Wang, Y. Shi, C. Sheng, S. Yang, P. He, H. Zhou, *Nat. Commun.*, 2024, **15**, 2263.
- [168] X. He, Z. Zhu, G. Wen, S. Lv, S. Yang, T. Hu, Z. Cao, Y. Ji, X. Fu, W. Yang, Y. Wang, *Adv. Mater.*, 2024, **36**, 2307599.

